The electronic structure of hcp lutetium

by

Timothy Alan Tibbetts

A Thesis Submitted to the

Graduate Faculty in Partial Fulfillment of the

Requirements for the Degree of

MASTER OF SCIENCE

Department: Physics

Major: Solid State Physics

Approved:

Members of the Committee:

_____

In Charge of Major Work

_____

_____

For the Major Department

_____

For the Graduate College

Iowa State University
Ames, Iowa

1982

TABLE OF CONTENTS

PAGE

INTRODUCTION 1

History and Motivation 1

Outline of Calculation 5

THE CALCULATIONAL METHODS 7

The APW and LAPW Methods 7

The RAPW and SO-LAPW Methods 11

The Exchange-Correlation Potential 17

The Muffin-Tin Approximation 20

The Susceptibility 21

The Form Factor 22

RESULTS AND COMPARISON WITH EXPERIMENT 24

RAPW vs. SO-LAPW Results 24

The Fermi Surface 28

The Susceptibility 43

The Specific Heat and Density of States 45

The Magnetic Form Factor 51

DISCUSSION AND CONCLUSIONS 59

APPENDIX : CALCULATIONAL DETAILS 62

REFERENCES 67

ACKNOWLEDGEMENTS 71

LIST OF TABLES

PAGE

TABLE 1. Orbital Areas 39

TABLE 2. Effective Masses 44

TABLE 3. Enhancement Factors 50

TABLE 4. The Neutron Magnetic Form Factor 58

LIST OF FIGURES

PAGE

FIGURE 1. Relativistic Energy Bands of Lu. This Calculation. 25

FIGURE 2. Relativistic Energy Bands of Lu. Keeton and Loucks. . . . 26

FIGURE 3. Folded out Fermi Surface of Lu. This Calculation. 30

FIGURE 4. Folded out Fermi Surface of Lu. Keeton and Loucks. 31

FIGURE 5. Fermi Surface of Lu. Full zone model. 33

FIGURE 6. Fermi Surface of Lu. Irreducible Wedge. 34

FIGURE 7. Extremal Orbits of Lu. 35

FIGURE 8. Experimental Angular Dependence of Orbits: 1010 Plane. . . 37

FIGURE 9. Experimental Angular Dependence of Orbits: 1120 Plane. . . 38

FIGURE 10. The α, β, and β-prime Orbits. 40

FIGURE 11. Theoretical Angular Dependence of the Orbits: 1010 Plane. 41

FIGURE 12. Theoretical Angular Dependence of the Orbits: 1120 Plane. 42

FIGURE 13. Webbing Feature in LHMK plane. 46

FIGURE 14. Theoretical Susceptibility Along z-axis. 47

FIGURE 15. Theoretical Density of States. 48

FIGURE 16. The Induced Neutron Magnetic Form Factor. 53

FIGURE 17. Energy Dependence of the Radial d Wavefunctions. 54

FIGURE 18. Angular Momentum Decomposition of the Charge Density. . . 57

FIGURE 19. One half hcp Unit Cell and Irreducible Wedge 64

INTRODUCTION

History and Motivation

The purpose of this investigation is to calculate the electronic structure of hcp lutetium, whose low temperature ground state is paramagnetic, thus providing a prototypical paramagnetic Fermi surface for the trivalent rare earth metals. Results obtained from the SO-LAPW (Linearized Augmented Plane Wave-including Spin-Orbit coupling)[1] method are compared with new de Haas-van Alphen (dHvA) measurements of the Fermi surface of lutetium[2], as well as susceptibility[3], specific heat[4-5], and form factor[6] measurements.

The number and quality of band structure calculations for the rare earths have been steadily increasing since the first non-self-consistent, non-relativistic, and non-spin-polarized calculation for Gd by Dimmock and Freeman[7] in 1964. Spurring this growth in the number of calculations is the wealth of experimental data which is becoming increasingly available, due both to new methods of crystal purification and to more sensitive experimental apparatus. Continuing refinement of band structure techniques, as well as a steady increase in available computational power, have provided the tools to produce band structure calculations which are both qualitatively and quantitatively in agreement with experiment. The early band structure calculations for the rare earths, beginning with the work of Dimmock, Freeman, and Watson in 1964, as well as the first fully relativistic but non-self-consistent Relativistic Augmented Plane Wave (RAPW) calculations of Keeton and

Loucks in 1965 (see the review by Freeman[8]), gave reasonably good agreement with the sparse experimental data then available. The available data were mainly from measurements such as neutron scattering and positron annihilation, which were less affected by impurities than more sensitive techniques for mapping the Fermi surface and measuring electronic properties, such as dHvA and magnetoresistance experiments. The most noticeable effects of relativity were the lowering of the s-bands relative to the d-bands, and the removal of most of the band crossings and degeneracies by the inclusion of spin orbit coupling. The correctness of these changes in the band structure, and hence in the Fermi surface, which were introduced by relativity, could not be assessed until more sensitive measurements could be performed on purer samples.

These early calculations showed that the rare earths were definitely not free electron-like, and, in fact, exhibited band structures similiar to those of the transition metals where the d-bands figure prominently. The f-bands were usually ignored in these calculations, mainly because it was uncertain whether the f-electrons could be adequately treated in terms of a band picture at all, due to their strong interactions. When an attempt was made to treat the 4f-bands realistically, their position relative to the Fermi level was found to be extremely sensitive to the chosen potential. Most available experiments for placing the 4f-bands, such as photoemission, still leave doubt as to the certainty of that placement. Additionally, since there was no ready way to treat these strong exchange and correlation effects

accurately, a standard average exchange approximation of the Slater alpha=1 form was generally used. The end result of using a strongly attractive interaction like this was to force the f-bands to lie well below the valence bands, since the f-bands are very localized, resulting in a larger exchange-correlation contribution than for the valence bands. Thus, the influence of the f-electrons on the valence bands, and hence upon the Fermi surface, was omitted. This was further rationalized by stating that the 4f-electrons were generally well isolated and localized, and should not be considered as valence bands. However, even though correlation is less important than exchange by a factor of 5-500 in non-rare earth atomic systems[9], and both are fairly well treated by an average exchange correlation potential, this is not true of systems with f-electrons. In general, f-electrons tend to be very strongly spin correlated, with both exchange and correlation effects being very important--often more important than some relativistic effects. This leads to an exaggeration of the inaccuracies introduced by the various local density exchange-correlation potential approximations. Since the 4f-electrons are highly spin correlated, spin polarized calculations are a realistic way of treating the open 4f-shell rare earths. The first spin-polarized band calculation, performed by Harmon and Freeman[10] on Gd within the Local Spin Density (LSD) approximation, gave results which are in fair agreement with dHvA experiments[11-13] and which lend hope for future work. It is possible that the inclusion of relativistic effects in the LSD formalism[14] will improve results. Since lutetium has a full 4f-shell, it avoids the need to consider this problem, allowing us to

focus attention on other aspects of the calculation.

Ideally, from a band structure point of view, all the electrons should be treated equivalently, in a self-consistent manner. Often, when a more rigorous physically accurate type of exchange-correlation potential is used, as discussed in Chapter 2, the actual placement of the f-bands becomes unstable in terms of self-consistency. We have found in the case of of lutetium, which has a closed 4f-shell (thus avoiding many of the problems involved in treating an open shell system where there are strong spin-dependent intra-atomic interactions among the f-electrons), when iterating to self-consistency, using a currently accepted exchange-correlation potential, that the 4f-bands tend to rise to the Fermi level. However, we have found that the actual location of the 4f-bands relative to the valence bands and the Fermi level seems to have little affect on the general features of the Fermi surface of lutetium, as long as the 4f-bands are not allowed to intersect the Fermi surface. This will not be true in other rare earths with partially filled 4f-shells, since, in a band picture, with narrow, highly localized 4f-bands, any partially filled 4f-bands by necessity lie near the Fermi level. A good example of this is cerium, in which the 4f-bands are located at the Fermi level, and are very much a factor in determining cerium's unique properties. It has also been hypothesized that lanthanum is superconducting, while isoelectronic yttrium and scandium are not, because the f-bands lie very close to, but above the Fermi energy in lanthanum, and the f-bands are involved in the enhancement of the electron-phonon pairing mechanism[15].

Outline of Calculation

In the first chapter, the SO-LAPW method is derived and discussed. The SO-LAPW method is a linearized, relativistic extension of the Augmented Plane Wave (APW) method of Slater[16], which provides a way of including the dominant non-spin-orbit relativistic effects as well as efficiently and accurately approximating spin-orbit coupling, while requiring much less computational effort than the full RAPW method of Loucks[17]. Choices of exchange-correlation potentials are examined, and the Hedin-Lundqvist potential, formulated within the Local Density (LD) approximation, is described. The effects of changes in the strength of the exchange-correlation potential are also discussed. The problems inherent in treating the 4f-bands, including their tendency to rise toward the Fermi level during a self-consistent calculation, and their sensitivity to the choice of the band center energy parameter are also discussed. Next, the limitations of the muffin-tin (MT) potential approximation are analyzed and evidence of the need for a general potential is presented. Finally, the theory of calculating the static q-dependent susceptibility and the induced neutron magnetic form factor is presented. In chapter two, the calculated band structure, density of states, susceptibility, Fermi surface, dHvA orbits including angular dependence,

and form factor are presented. These results are compared to the experimental results and the results of previous non-self-consistent RAPW calculations by Keeton and Loucks[18-19] and by Stassis et al.[6], in which the alpha=1 exchange correlation potential was used, thus keeping

the 4f-bands below the valence bands and avoiding interaction effects. Conclusions and directions for future work are summarized in chapter three. Details of the various calculations are contained in the Appendix.

THE CALCULATIONAL METHODS

The APW and LAPW Methods

In considering the APW Method and its extensions, it should be kept in mind that several assumptions, which are commonly made to simplify the general problem of solving Schroedinger's equation in a solid, can have adverse effects upon the resultant band structure. First, we make use of the Born-Oppenheimer approximation, which allows separation of the treatment of the electrons and ions, i.e., ignoring the electron-phonon interaction. One result of this approximation is a calculated density of states at the Fermi level which is too low when compared with the low temperature linear term in specific heat measurements. This requires the inclusion of an electron-phonon enhancement factor to make up the difference. Secondly, we assume that the electrons move in an effective Coulomb or Hartree field, i.e., as a first approximation we ignore correlations between electrons and assume they are approximately independent. However, some effort is made to include exchange and correlation effects in a combined exchange-correlation potential, as will be discussed later. Treating the exchange potential exactly, as in the Hartree-Fock method, results in a nonlocal expression. The usual simplification involves reducing the nonlocal problem to a local one via

some formulation of the Local Density Approximation (LDA) or the Local Spin Density Approximation (LSD), depending on whether the calculation is spin-polarized or not, which will be discussed in section three of this chapter.

It is quite remarkable that it is at all possible to calculate a realistic band structure, in light of the gross approximations that must be made in order to deal with a highly correlated and inhomogenous system of 10^{23} electrons. The reason that it is possible to handle this potential Pandora's Box is the fortuitous fact that we are actually dealing with a system of quasiparticles, i.e., particles which consist of an electron and its exchange-correlation hole. These quasiparticles are electrically neutral and behave in an approximately independent manner. Thus, working in terms of the quasiparticles allows us to reduce a many body problem to a single body problem with some justification, as well as allowing us to achieve reasonably good results.

The APW method is a way of solving the Schroedinger (or Dirac) equation variationally, which was suggested by John C. Slater[16] in 1937, as an easier way to calculate the electronic structure of solids than the only other procedure then available, the cellular method. The APW method overcame the difficulties of satisfying periodic boundary conditions inherent in the cellular method. However, APW calculations were not particularly feasible until the early 1960s because of the large amount of computation involved.

The essence of the APW method involves the partitioning of the unit cell into two separately treated regions, a spherical region around each ion, and the remaining interstitial region. A further simplification generally used is the Muffin-Tin (MT) approximation, first suggested by Slater[20] in 1935, in which the potential is assumed to be spherically symmetric inside the MT spheres around each ion, and equal to a constant, which can be set equal to zero by shifting the energy, in the interstitial region. One then proceeds to solve Schroedinger's equation by use of the variational principle. We will arrive at our final solution by means of minimizing the energy in a variational expression, so we require a variational function:

$$\phi = \sum_i C_i \chi_i \tag{1}$$

where the χ_i are the APW basis functions. The solution of Schroedinger's equation inside the sphere for a given MT potential is given by a product of spherical harmonics and radial functions which satisfy the radial part of Schroedinger's equation. In the interstitial region, the solutions are the solutions to Schroedinger's equation with zero potential, which are plane waves. Thus, we use a dual representation for our variational function. Inside the MT sphere, we take the atomic-like solutions:

$$\chi(E) = \sum_{l,m} A_{lm} Y_l^m R_l(E) \tag{2}$$

In the interstitial region we take plane waves:

$$\chi = e^{(i\underline{k}\cdot\underline{r})} \tag{3}$$

Thus, the basis functions for the variational expression are

augmented plane waves, and hence the name of the method. One generally matches the values of the two sets of variational functions at the MT boundary by means of a Rayleigh expansion of the plane waves in terms of spherical harmonics which determines the coefficients A_{lm}. One should note that the derivatives of the functions are allowed to be discontinous at the MT boundary. Next, we form a variational expression for the energy in terms of ϕ, and then minimize the energy with respect to the expansion coefficients C_i, which results in a determinental equation to be solved:

$$\det| M(E)_{ij} | = \det| H(E)_{ij} + S(E)_{ij} - E \cdot D(E)_{ij}| = 0 \qquad (4)$$

where H is the MT Hamiltonian, S is a surface term which represents the contribution to the kinetic energy from the remaining discontinuity in the slope of the variational function at the MT boundary, and D is an overlap matrix. This is a less convenient form of secular equation to solve than the standard eigenvalue-eigenvector type problem. The solution is more difficult since it requires searching the determinant as a function of energy to find its zeros, due to the implicit dependence of the APW functions themselves inside the MT spheres upon the energy. Furthermore, the secular equation for the determinant contains singularities.

The LAPW method was developed by Andersen[21] and Koelling and Arbman[22] to help remove these problems. In the LAPW method, one proceeds in essentially the same manner as in the APW method, except for the inclusion of an energy derivative in the radial equations, i.e., one

expands R_l in a Taylor series about some energy parameter E_o. The basis functions inside the MT then look like:

$$\chi = \sum_{l,m} [A_{lm} R_l + B_{lm} dR_l/dE] Y_l^m \qquad (5)$$

Then, one uses the additional variational freedom included by the derivative term to match both the functions and their derivatives at the MT boundary, which eliminates the surface terms in the variational expression for the energy. Furthermore, the energy can now remain fixed within a fairly wide region, rather than requiring the search of the determinant for zeroes over a range of energies. Some care is still required in choosing the energy parameter E_o, particularly for states of higher angular momentum, which tend to be more localized[23]. The beauty of the LAPW method is that it allows one to obtain the eigenvalues in a single matrix diagonalization with only a minimal increase in the effort needed to set up the matrix.

The RAPW and SO-LAPW Methods

In 1965, Terry Loucks[17] extended the APW method by including relativity, thus creating the RAPW method. In the RAPW method, the procedure is to solve the Dirac equation using a muffin-tin potential. There are two main reasons for wanting to avoid the use of this full formalism. First, the exchange interaction between valence electrons is

usually larger than the spin-orbit contribution. It is particularly important in the case of open 4f-shells. Thus, it is reasonable to keep spin as a good quantum number to facilitate the handling of the exchange interaction, while still taking the spin-orbit interaction into account in some reasonable way. In the case of lutetium, the exchange interaction is still large but not as important, since the 4f-shell is full. Secondly, since both spin states are included, the resulting matrix to be diagonalized has dimensions twice as large as the corresponding non-relativistic matrix and becomes complex as well, which increases the computational time required by nearly an order of magnitude. However, in the SO-LAPW method, even though true self-consistency requires the inclusion of all relativistic effects in every iteration, it should be noted that the inclusion of spin-orbit coupling does not change the charge density very much. Hence, one can solve this complex, expanded matrix only once, during the final iteration, rather than during every iteration, as in the RAPW method, and still get good results. In addition, one can include the spin-orbit interaction within only a small number of bands of interest, which substantially decreases the size of the matrix to be diagonalized.

The essence of the SO-LAPW method is the implementation of the Koelling-Harmon[24] technique for the variational solution of the Dirac equation, in terms of the LAPW formalism previously described, while including pure spin basis functions in the large component of the wavefunction. To see where the approximation enters the calculation,

first recall the total Hamiltonian of the system:

$$H = c\,\underline{\alpha} \cdot \underline{p} + (\beta - 1)mc^2 + V(\underline{r}) \tag{6}$$

where the energies are measured relative to the rest mass energies. The solution inside the MT sphere is of the form:

$$\Phi_{\kappa\mu} = \begin{bmatrix} G_\kappa\, \chi_{\kappa\mu} \\ -i\, F_\kappa\, \sigma_r\, \chi_{\kappa\mu} \end{bmatrix} \tag{7}$$

where:

$$\chi_{\kappa\mu} = \sum_m C(\iota\tfrac{1}{2}j;\mu-m,m)\, Y_\iota^{\mu-m}\, \chi_m$$

$$\kappa = \iota\,, \qquad j = \iota - \tfrac{1}{2}$$

$$\kappa = -(\iota + 1)\,, \quad j = \iota + \tfrac{1}{2}$$

$$\sigma_r = \underline{r} \cdot \underline{\sigma}$$

with F_κ and G_κ satisfying the radial equations:

$$dF_\kappa/dr = (1/c)(V-E)G_\kappa + ((\kappa-1)/r)F_\kappa \tag{8}$$

$$dG_\kappa/dr = -((\kappa+1)/r)G_\kappa + 2McF_\kappa \tag{9}$$

where $M = m + (1/2c^2)(E-V)$

If we now let $P_\kappa = rG_\kappa$ and $Q_\kappa = rF_\kappa$ the radial equations become:

$$dP_\kappa/dr = (-\kappa/r)P_\kappa + 2McQ_\kappa \tag{10}$$

$$dQ_\kappa/dr = (1/c)(V-E)P_\kappa + (\kappa/r)Q_\kappa \tag{11}$$

Now, if we write out the above two equations for the two possible values of κ, $\kappa=\iota$ and $\kappa=-\iota-1$, and then add and subtract appropriate

combinations, we arrive at the following set of differential equations:

$$d\Phi_\iota/dr - \Phi_\iota/r = 2Mc\Gamma_\iota + \iota(\iota+1)\delta\Phi_\iota/(2\iota+1)r \tag{12}$$

$$d\Gamma_\iota/dr - \Gamma_\iota/r = (V-E)\Phi_\iota/c - \iota(\iota+1)\delta\Gamma_\iota/(2\iota+1) \tag{13}$$

$$d\delta\Phi_\iota/dr = (2\iota+1)\Phi_\iota/r + 2Mc\delta\Gamma_\iota \tag{14}$$

$$d\delta\Gamma_\iota/dr = (V-E)\delta\Phi_\iota - (2\iota+1)\Gamma_\iota/r \tag{15}$$

where the following average and difference function definitions were used:

$$(2\iota+1)\ \Phi_\iota \equiv \iota\ P_\iota + (\iota+1)\ P_{-\iota-1} \tag{16}$$

$$(2\iota+1)\ \Gamma_\iota \equiv \iota\ Q_\iota + (\iota+1)\ Q_{-\iota-1} \tag{17}$$

$$\delta\Phi_\iota \equiv P_{-\iota-1} - P_\iota \tag{18}$$

$$\delta\Gamma_\iota \equiv Q_{-\iota-1} - Q_\iota \tag{19}$$

For convenience let Φ and Γ go to P and Q and drop the ι subscript. Now, the approximation consists of assuming that the derivative of the difference in the large component of the wavefunction is very small, i.e., assume:

$$d\delta P/dr \simeq 0 \tag{20}$$

Then:

$$\delta Q \simeq -(2\iota+1)P/(2Mcr) \tag{21}$$

Substituting this result into equation (13), we have

$$dQ/dr + Q/r = (V-E)P/c + \iota(\iota+1)P/(2Mcr^2) \tag{22}$$

And, if we assume $\delta P = 0$ as well, we have[24] :

$$dP/dr - P/r = 2McQ \tag{23}$$

$$dQ/dr + Q/r = [(V-E)/c + \iota(\iota+1)/(2Mcr^2)]\ P \tag{24}$$

And our former solution $\Phi_{\kappa\mu}$ inside the MT sphere becomes:

$$\phi_{\iota ms} = 1/r \begin{bmatrix} P_\iota \, Y_\iota^m \, \chi_s \\ i\sigma_r \, [-Q_\iota + (P_\iota/2Mcr)\underline{\sigma}\cdot\underline{L}] \, Y_\iota^m \, \chi_s \end{bmatrix} \tag{25}$$

The net result of this approximation is to give a pure spin function in the large component, although there is still a mixture of spin in the small component. A good further approximation[24] is to neglect the small component.

Now, if we want to develop the LAPW method in this context, we include the first energy derivative:

$$d\phi/dE \simeq 1/r \begin{bmatrix} dP_\iota/dE \, Y_\iota^m \, \chi_s \\ \sigma_r[-dQ_\iota/dE + (dP_\iota/dE/2Mcr)\underline{\sigma}\cdot\underline{L}] \, Y_\iota^m \, \chi_s \end{bmatrix} \tag{26}$$

where dP/dE and dQ/dE satisfy the energy derivative version of the radial equations:

$$d^2P/dEdr - (1/r)dP/dE = 2McdQ/dE + Q/c \tag{27}$$

$$d^2Q/dEdr + (1/r)dQ/dE = [\iota(\iota+1)/2Mcr^2 + (V-E)/c]dP/dE - P/c \tag{28}$$

where higher order terms have been neglected in both of the above equations. The required normalization condition is:

$$\int_0^R dr \, (P \, dP/dE + Q \, dQ/dE) = 0 \tag{29}$$

Then:

$$H\, d\phi/dE = \varepsilon\, d\phi/dE + \phi + H_1^{so}\, d\phi/dE \tag{30}$$

where:

$$H_1^{so}\, d\phi/dE = (1/2Mcr)^2\, dV/dr\, (dP/dE - P/4Mc^2)\, \Xi$$

and:

$$\Xi = \begin{bmatrix} \sigma \cdot L\, Y_l^m\, \chi_s \\ \\ 0 \end{bmatrix}$$

The general procedure from this point is to temporarily ignore the matrix elements of H_0^{so} and H_1^{so}, thereby including most of the relativistic effects in the iterations to self-consistency, then include the spin-orbit effects in the final iteration. One performs a standard variational procedure to arrive at a secular equation of the form:

$$H\, \underline{c} = E\, \underline{S}\, \underline{c} \tag{31}$$

where: $H_{n's',ns} = H^{sr}_{n',n}\delta_{s',s} + H^{so}_{n's',ns}$

and: $S_{n's',ns} = S^{so}_{n',n}\delta_{s',s}$

where sr stands for semirelativistic. The total spin-orbit matrix elements are then expressible as:

$$H^{so}_{n's',ns} = 4\pi \sum_{l,m,m'} R^l_{n',n}\, \Xi\, Y_l^{m'}(\hat{k}_{n'})\, Y_l^m(\hat{k}_n) \tag{32}$$

where:

$$R^l_{n',n} = (4\pi R^4/\Omega)\, [\, AA\, \xi 0 + AB\, \xi 1 + BB\, \xi 2\,]$$

$$\Xi = \chi^*_{s'} \int d^2r\, Y_l^{m'*}\, \underline{\sigma} \cdot \underline{L}\, Y_l^m\, \chi_s$$

and:

$$\xi 0 = {}_0\int^R dr\ P_l^{\,2}(1/2Mc)^2\ (1/r)\ (dV/dr)$$

$$\xi 1 = {}_0\int^R dr\ P_l\ dP_l/dE\ (1/2Mc)^2\ (1/r)\ (dV/dr)$$

$$\xi 2 = {}_0\int^R dr\ (dP_l/dE)^2\ (1/2Mc)^2\ (1/r)\ (dV/dr)$$

and:

$$AA = A_l(k_n)\ A_l(k_{n'})$$

$$AB = A_l(k_{n'})\ B_l(k_n) + B_l(k_{n'})\ A_l(k_n)$$

$$BB = B_l(k_{n'})\ B_l(k_n)$$

One then solves the secular equation using H^{sr} and S^{sr} to obtain self-consistent solutions with coefficients and energies C_n^{sr} and ε_j^{sr}. Then, using the new basis set:

$$\phi_{js} = \sum_n C_n^{sr}(\varepsilon_j^{sr})\ P(k_n s;r) \quad , \quad \varepsilon_j^{sr} < \varepsilon_j^{max} \tag{33}$$

one solves a second secular equation including the previously neglected spin-orbit matrix elements H_0^{so} and H_1^{so} to get the relativistic results including approximate spin-orbit effects.

The Exchange-Correlation Potential

In order to make the self-consistent independent electron equations easier to solve, some approximation must be made for the nonlocal exchange contributions. The earliest attempts to take exchange and correlation effects into account in band calculations, i.e., to include some many-body effects in the single body equations, were based upon

Thomas-Fermi type local density approximations, where the exchange correlation potential is assumed to be a function of the local charge density. The best known approximation of this type is Slater's statistical exchange $\rho^{1/3}$ potential[25] which was originally of the form:

$$V_{xc}(r) = -(3/2\pi)\ (3\pi^2\rho(r))^{1/3} \tag{34}$$

However, Gaspar[26] and later Kohn and Sham[27], rederived Slater's exchange potential with a coefficient two thirds as large:

$$V_{gks}(r) = 2/3\ V_{xc}(r) \tag{35}$$

Then Slater and Johnson[28], and soon many others, began using the so called Slater Xα approach, where:

$$V_{X\alpha}(r) = \alpha\ V_{xc}(r) \tag{36}$$

where α is usually between 2/3 and 1, and is often chosen such that the resultant atomic ground state energy is precisely the energy obtained from the Hartree-Fock method. However, it should be noted that the atomic system differs considerably from the solid, mainly in that the atom has a large low-density region. The Xα method is mainly a high-density approximation, which is corrected for the low-density atomic regions by the adjustment of α. Hence, the best choice of α for the atom is probably not the best choice for the solid, which does not have a large low-density region. Furthermore, the Hartree-Fock method does not include Coulombic correlation, but only Pauli (like spin) correlation. In addition, this is still a crude method, which allows adjustment of α without regard for the physics.

A better and more physical approximation with no adjustable parameters is that of Hedin and Lundqvist[29] :

$$V_{xc}(r) = \beta(r)\, V_{gks}(r) \qquad (37)$$

This formulation is based upon the theorems of Hohenberg and Kohn[30], which exploit the aforementioned concept of a system of nearly independent quasiparticles. These two theorems, which form the basis of all density-functional theories, show that for an inhomogenous, interacting electron gas, e.g., the electrons in a solid, the ground state properties such as bulk modulus, wavefunctions, etc., are unique functionals of the electronic density, and that the total energy of the system is a minimum for the correct density. Here, the β function is essentially an extrapolation between high- and low-density results for an interacting electron gas, where the results can be more easily and accurately calculated. In fact, the Hedin-Lundqvist results are exact in the limit of high- and low-densities.

In this calculation, the Hedin-Lundqvist exchange-correlation potential was used, in the hope that it would help stabilize the position of the 4f-bands. However, it has been observed, that exchange-correlation approximations based upon the local density-functional approach generally treat localized bands incorrectly. The more localized a band is, the more likely that its calculated energy will be too high relative to the Fermi level[31]. In the case of transition metal d-bands, this error is on the order of 1 eV or less. However, with f-bands, which are extremely localized, the error could be much greater and could be

the major source of instability in the f-bands of lutetium. Much work has been done in attempting to develop local-density or average-density-type approaches that treat these localized and highly correlated bands more accurately[32], but a successful application to solid systems has yet to be presented.

The Muffin-Tin Approximation

Insofar as the potential is concerned, one has a choice of essentially three different levels of approximation for use in band structure calculations. First, one can use a muffin-tin (MT) approximation as previously described, which in fact most rare earth calculations have used, with fair results. The more detailed Fermi surface studies by dHvA and magnetoresistance methods are beginning to show the need for better potential approximations. The second choice is the Warped MT (WMT) approximation[12,33-35], which allows the interstitial potential to vary, rather than remain constant. This has been used for rare earth systems and can account for a 5 to 10 mRy difference in the band energies[36]. The third and most difficult option is the general potential[34-37], in which one includes nonspherical contributions inside the MT sphere, as well as WMT effects in the interstitial region. This method has been used on fcc and bcc transition metals[38-40], and has, in

general, resulted in changes in the band energies of 5-15 mRy from their MT values.

The Susceptibility

We are concerned with the relationship between the magnetic ordering wave vectors of the heavy rare earths and certain general features of the Fermi surface. If we apply a spatially varying magnetic field to a metal, and assume that the response of the electron gas in the solid is linear, we find that the relationship between the field and the response of the magnetic moments in the solid is governed by the generalized susceptibility:

$$M(\underline{q}+\underline{G}) = \sum_{G'} \chi(\underline{q}+\underline{G}',\underline{q}+\underline{G})\, B(\underline{q}+\underline{G}') \qquad (38)$$

We will use the standard result[41], and ignore temperature and frequency dependence:

$$\chi(\underline{q}) = \sum_{n,n',k} | M_{nn'}(\underline{q},\underline{k}) |\, f_n(\underline{k})[1-f_n(\underline{k}+\underline{q})]/[E_{n'}(\underline{k}+\underline{q})-E_n(\underline{k})] \qquad (39)$$

We make the further approximation that the matrix elements $M_{nn'}$ are constant, and then convert the sum into an integral over the Brillouin zone. The integral is performed by the tetrahedron method[42], in which the irreducible piece of the Brillouin zone is divided into a large number of small tetrahedra, inside each of which the integral is performed analytically by the use of linear interpolation, in which we

calculate the energy at each of the four corners of the tetrahedra, and assume that the Fermi surface intersects the tetrahedra in a flat plane.

The relationship between the susceptibility and a general ordering vector Q comes from the proportionality of the susceptibility to the negative of the magnetic interaction energy. Thus, the maximum in the susceptibility corresponds to the minimum in the energy, and hence corresponds to the wave vector Q which stabilizes the magnetic ordering. In the case of lutetium, which is paramagnetic, the experimental Q must be determined from extrapolations of measurements on dilute alloys of lutetium and other magnetic rare earths. Finally, one additional result, which serves as a check on the consistency of the theoretical results, is the required limiting behavior of the susceptibility, in the case of constant matrix elements:

$$\lim_{q \to 0} \chi(q) = (1/2)\, N(Ef) \qquad (40)$$

where N(Ef) is the density of states at the Fermi level.

The Form Factor

To the extent that the spin contribution is dominant, the induced neutron magnetic form factor of a metal allows a good test of the quality of the important wavefunctions at the Fermi level which are generated in a band structure calculation. The form factor is the

Fourier transform of the magnetization density and consists of both spin and orbital contributions. Generally, the spin part tends to dominate the total form factor. In fact, the atomic spin form factor, by itself, is often in very good agreement with experimental results. For a ferromagnetic system, the spin magnetization density is the difference between the spin up and the spin down densities. In paramagnetic systems, which exhibit only a very small induced magnetic moment, even at high applied fields, the spin density is taken as the density of the spin up states at the Fermi level which have corresponding unoccupied spin down states. Then, the spin density is given by:

$$\rho(r) = C \sum_{n} \int_{E=Ef} (dA_n(k)/|\nabla E_n(k)|) \; |\Psi|^2 \qquad (41)$$

where the integral is over energies at the Fermi level only. The spin form factor is[43]:

$$F_{spin}(\underline{G}) = \int d^3r \rho(r) \; e^{(-i\underline{G}\bullet\underline{r})} \qquad (42)$$

The calculational details are discussed in the Appendix.

RESULTS AND COMPARISON WITH EXPERIMENT

Until recently, a detailed, experimentally-determined Fermi surface for lutetium has been lacking, mainly due to the extremely pure samples required, which were not readily available. The chemically similar valence of the 4f rare earth metals as well as their tendency to absorb small impurities makes separation and purification difficult. However, the development of zone refining and electrotransport techniques in the last ten years has resulted in increasingly pure rare earth samples. In the first section, results of this calculation are compared with results of an early RAPW calculation by Keeton and Loucks[18-19]. In section two, the theoretical and experimental Fermi surfaces are compared. Susceptibility calculations are compared with experiment in section three. Section four compares the calculated density of states with specific heat measurements. In section five, the calculated form factor is compared with experimental results and with a previous, non-self-consistent RAPW form factor calculation.

RAPW vs. SO-LAPW Results

As shown in Figures 1 and 2, the band structure of this calculation is very similar to the RAPW band structure of Keeton and Loucks. Since Keeton and Loucks used the Slater α=1 exchange, their 4f-bands ended up below the valence bands and are not shown. The 4f-band placement shown for this SO-LAPW calculation is not certain. The results shown, which will be referred to as the results of potential one (POT1), are the result of a series of iterations in which the Fermi energy had

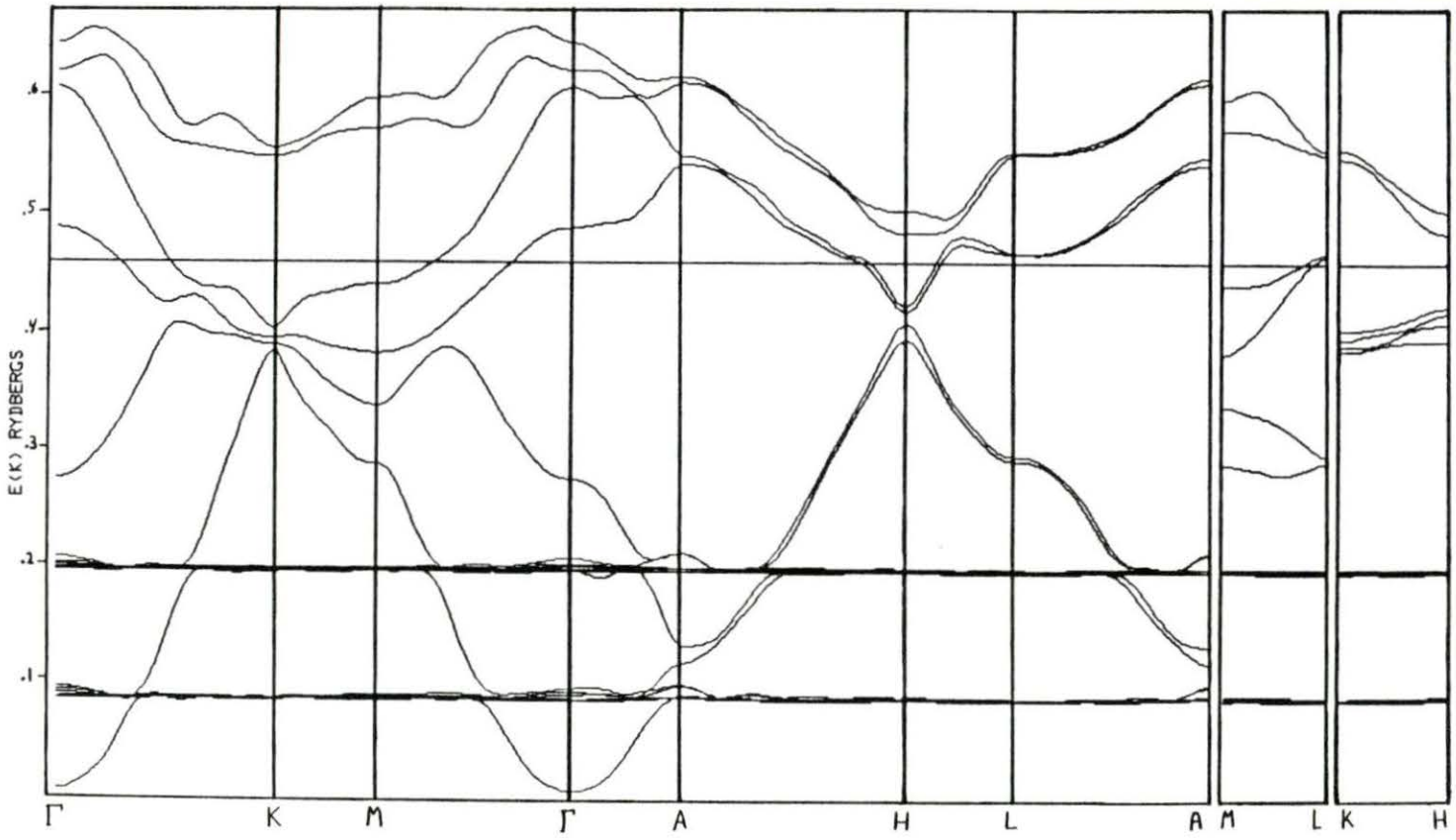

FIGURE 1. Relativistic Energy Bands of Lu. This Calculation.

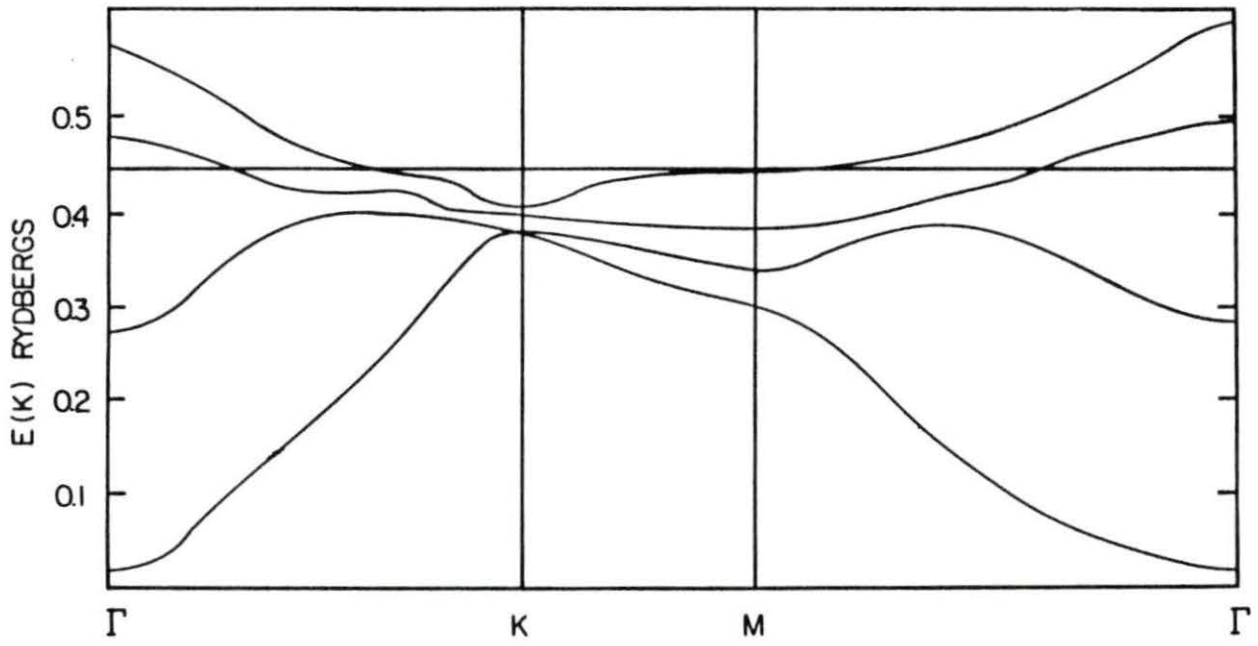

FIGURE 2. Relativistic Energy Bands of Lu. Keeton and Loucks.

of the 4f-bands, the results seem to indicate that the 4f-bands are well below the Fermi level. However, even though one might therefore expect the Fermi surface of Keeton and Loucks to be quite similar to the Fermi surface of this calculation, it should be kept in mind that an $\alpha=1$ exchange generally has the effect of narrowing the d-bands and producing a relative d-s shift, in addition to pulling down the 4f-bands, which could change the Fermi surface significantly, as will be discussed in the next section. Furthermore, it has been noticed that a non-self-consistent calculation performed with a strong exchange-correlation potential, such as the Slater $\alpha=1$, usually produces bands near the Fermi energy which are quite similar to the results of self-consistent calculations using a weaker, e.g., $\alpha=2/3$-type of potential. However, the wavefunctions, and hence the form factor, are much more sensitive to self-consistency and the chosen potential than are the energy bands, as will be discussed in section five.

The Fermi Surface

One of the most precise tools available for accurately examining the Fermi surface of metals is the dHvA effect, which is based upon the fact that the orbits of the band electrons become quantized Landau orbits in the presence of a strong magnetic field. As the field strength is changed, the orbits with energies near the Fermi energy move through the Fermi level, resulting in the population or depopulation of certain orbits in a discontinous, quantized fashion. The result is an oscillation in the magnetic moment of the metal, which is periodic in

the inverse of the magnetic field strength. This frequency is proporional to the extremal cross-sectional area of the Fermi surface perpendicular to the field direction. Thus, measuring frequency as a function of field direction produces a graph of orbital areas as a function of field direction, which provides a detailed map of the extremal areas of the Fermi surface.

An early attempt at mapping the Fermi surface of lutetium via dHvA orbits by Hoekstra and Phillips[45], using a sample with a resistivity ratio (ρ(300K)/ρ(4.2K) of 60 and pulsed fields of up to 200 kilogauss, resulted in the discovery of only one orbit. However, a recent study by Johansen, Crabtree, and Schmidt[2], using a lutetium sample with a resistivity ratio of 100, as well as a new experimental apparatus which allowed them to reach a higher field-to-temperature ratio (field 150kg, temperature .3K) than Hoekstra and Phillips, resulted in the discovery of eight distinct orbits. Unfortunately, a small misalignment problem may have affected some of the results of Johansen et al., particularly around the H point. Hoekstra and Phillips found only a single orbit around the H point, while Johansen et al. found two orbits. The RAPW calculation of Keeton and Loucks predicts two orbits in this region, but not the same two as were found by experiment, which show a different angular dependence. This calculation predicts three distinct orbits at this point. These calculational differences are illustrated in the folded out Fermi surfaces of Figures 3 and 4 .

In the RAPW Fermi surface, the electron sheet (inner surface) along the HK direction is cylindrical, which means that it can support only

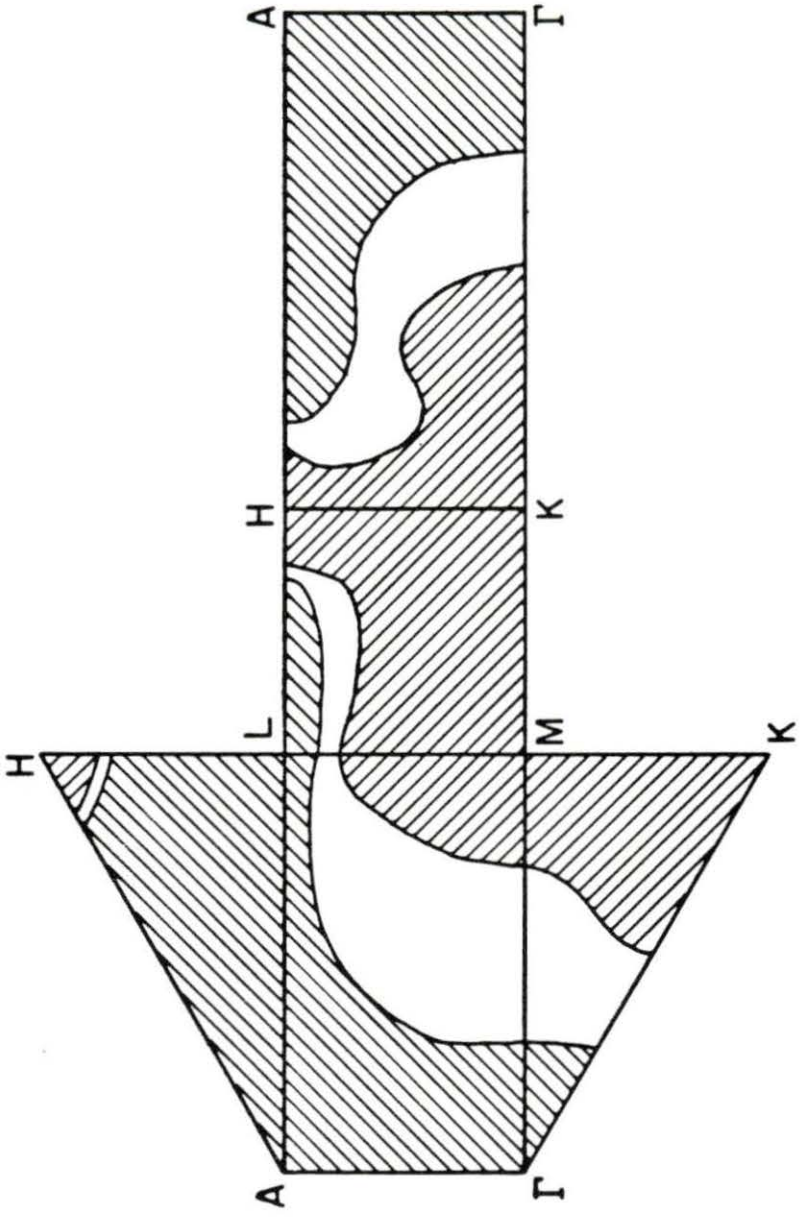

FIGURE 3. Folded out Fermi Surface of Lu. This Calculation.

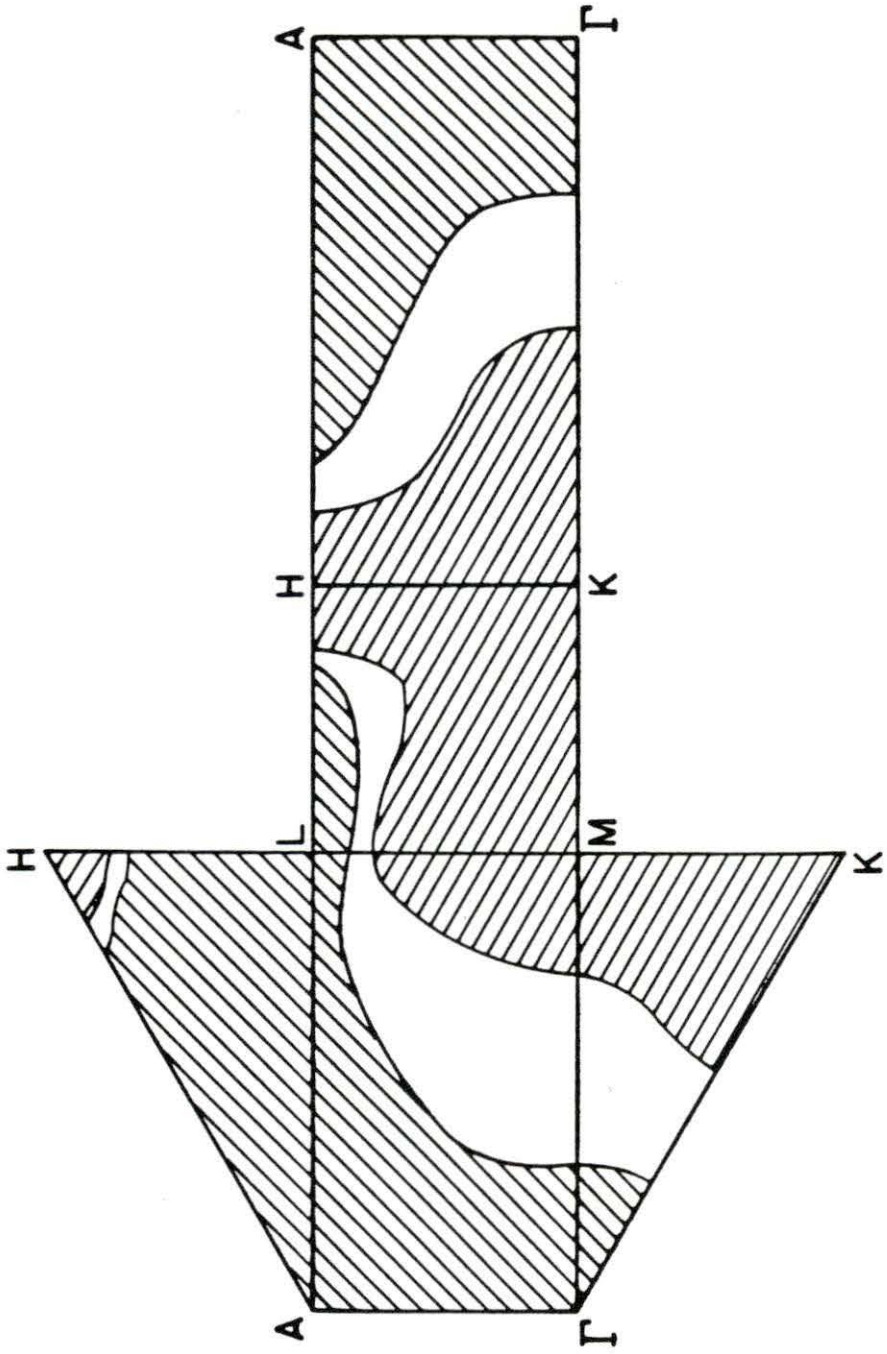

FIGURE 4. Folded out Fermi Surface of Lu. Keeton and Loucks.

one extremal orbit. However, the SO-LAPW electron surface exhibits both a neck and a belly, i.e., both a minimum and a maximum area, which will support two extremal orbits. Both calculations show a second cylinder due to the hole sheet, which will support one orbit, which was not found experimentally by Johansen et al. The second main difference between the RAPW and SO-LAPW results is the lack of a "nose" in the Γ-K-H-A plane of the RAPW hole surface. This nose does not appear to make any noticeable change in the extremal orbits. The other six orbits agree reasonably well with theory and, we believe, fully map out the remainder of the Fermi surface, insofar as extremal orbits are concerned.

Shown in Figures 5 and 6 are full zone and irreducible wedge models of the Fermi surface consisting of hole and electron sheets, due to the third and fourth bands crossing the Fermi level. The nine predicted extremal orbits, five on the electron sheet and four on the hole sheet, are marked on the irreducible wedge model. The shapes of the nine orbits are shown in Figure 7. Table 1 contains the extremal orbit areas found experimentally by Hoekstra and Phillips and by Johansen, Crabtree, and Schmidt, as well as the theoretical areas determined by this calculation, for the two different potentials. It should be noted that the two different potentials with different placements of the 4f-bands give quite similar results. Also included in Table 1 are the areas estimated from the folded out Fermi surface of Keeton and Loucks (Figure 4) by Johansen et al., as well as the the semirelativistic (fully relativistic without spin-orbit coupling) results of this calculation. The semirelativistic (SR) results show that, except for splitting the

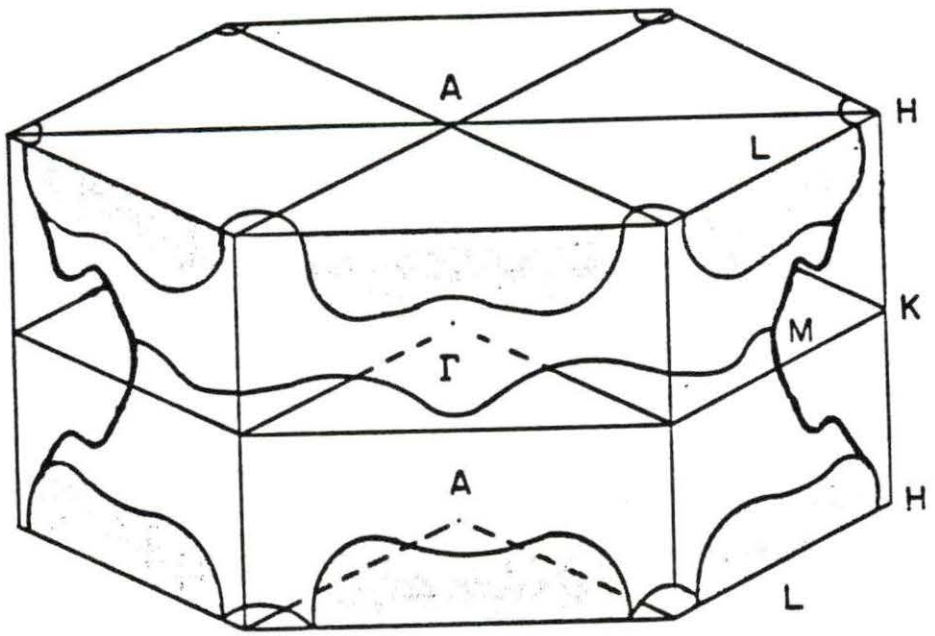

a.

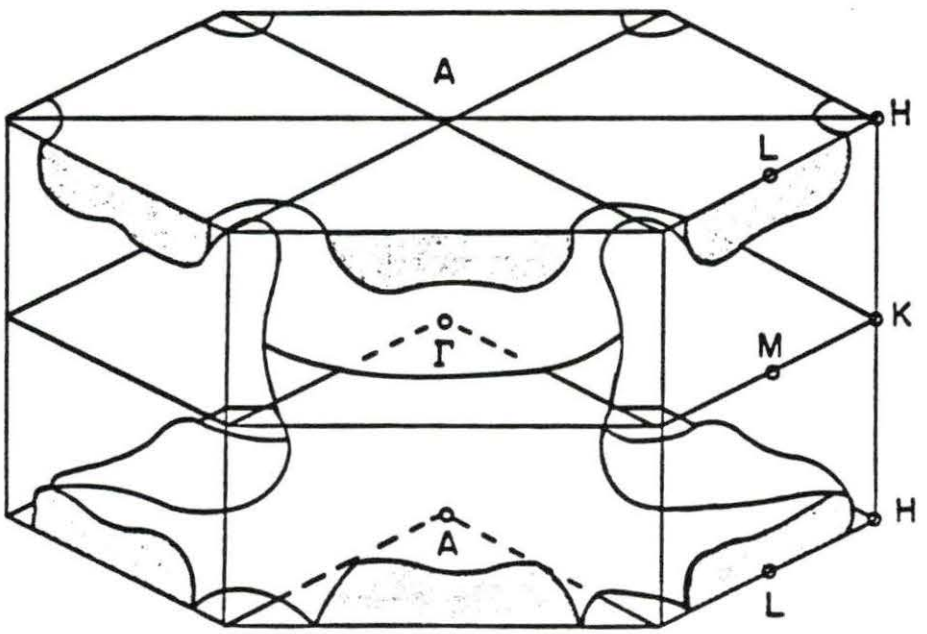

b.

FIGURE 5. Fermi surface of Lu. a:Electron sheet. b:Hole sheet.

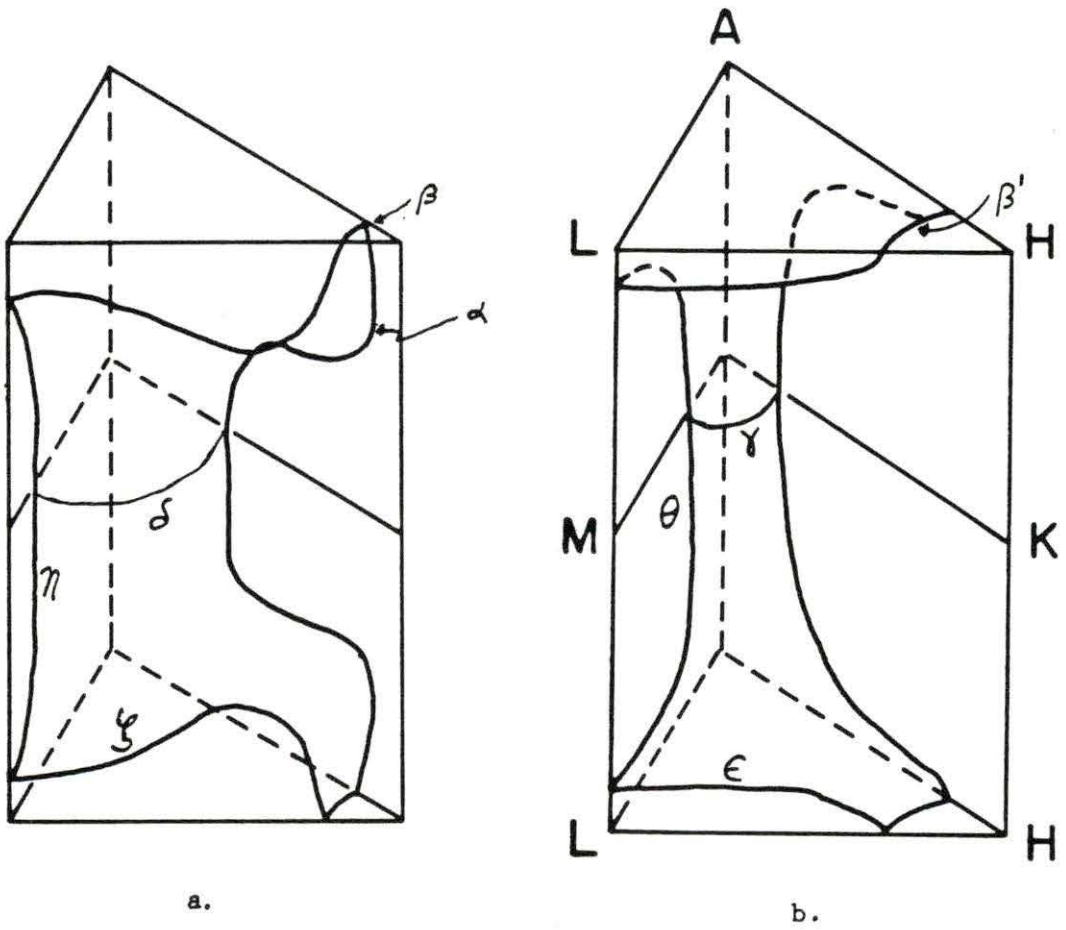

FIGURE 6. Fermi surface of Lu. a:Electron sheet. b:Hole sheet.

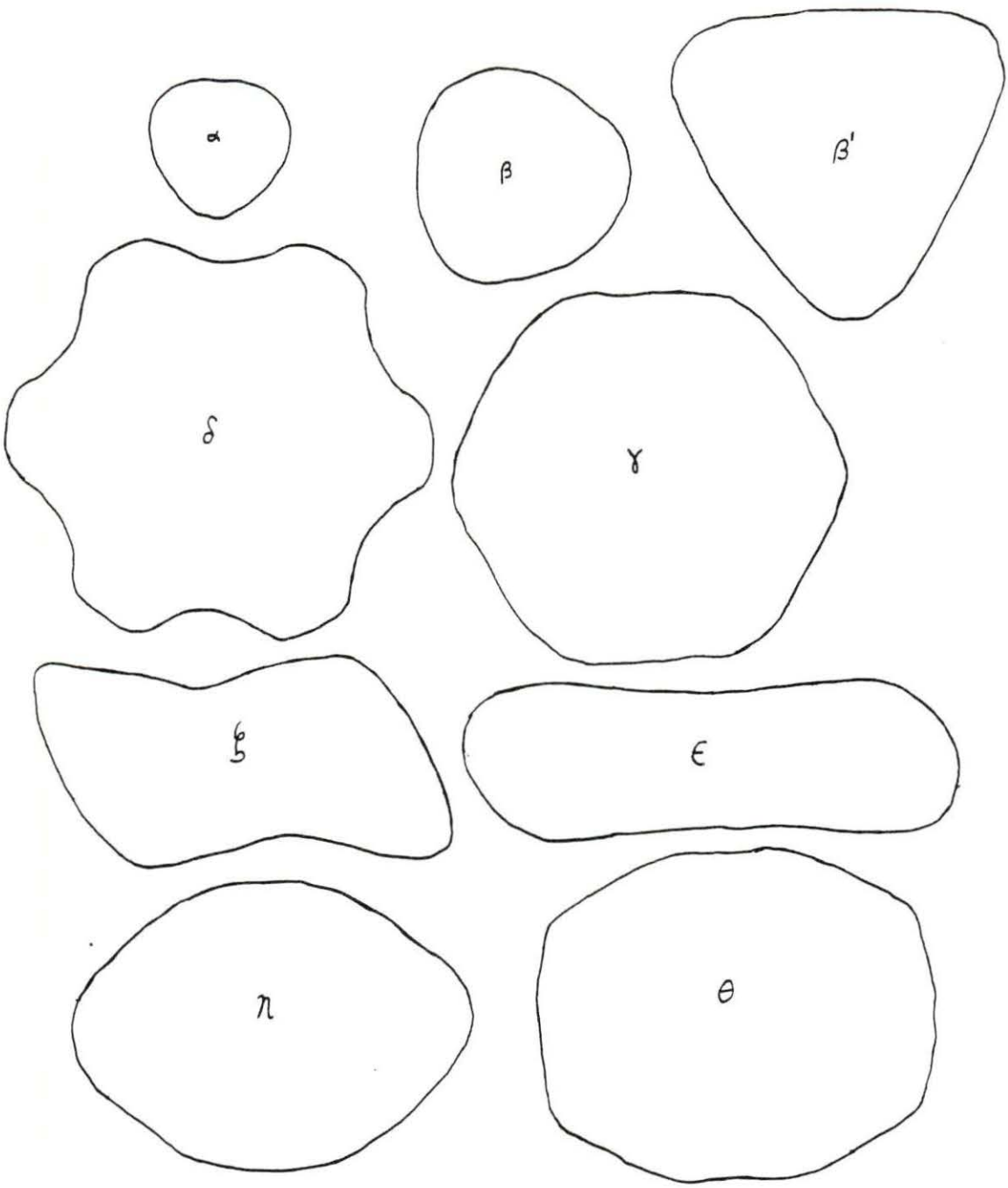

FIGURE 7. Extremal Orbits of Lu.

degeneracy of bands three and four on the AHL plane thus giving rise to three orbits around the H point rather than one, the inclusion of spin-orbit coupling really didn't affect the larger orbits, i.e., the gross features of the Fermi surface.

The areas from this calculation are in generally good agreement with experiment, except for the small α and β orbits around the H point. As can be seen from the experimental angular dependence measurements of these orbits in Figures 8 and 9, some odd behavior is in evidence, possibly due to the misalignment problem mentioned earlier. An interesting and previously unreported theoretical result is the shape of the Fermi surface around the H point, shown in Figure 10, which explains the branching together of the α and β orbits seen in Figures 8 and 9. With the magnetic field along the HK direction, two distinct orbits are observed on the electron sheet. As the field is tilted, the larger belly orbit decreases in area, while the smaller neck orbit increases in area. Eventually, when the field is tilted about 25 degrees from the c-axis, the two orbits become degenerate, forming one larger orbit. It is believed that the single orbit found by Hoekstra and Phillips corresponds to the α orbit. Their orbit disappeared at a field tilt of 22 degrees, which is consistent with the results one would expect from a less pure sample. The β orbit has a larger area, and the two orbits do not merge until the field is tilted approximately 25 degrees. Additionally, both the theoretical and experimental areas and masses of the α orbit are in good agreement.

The correct angular dependence of the Johansen et al. orbits is

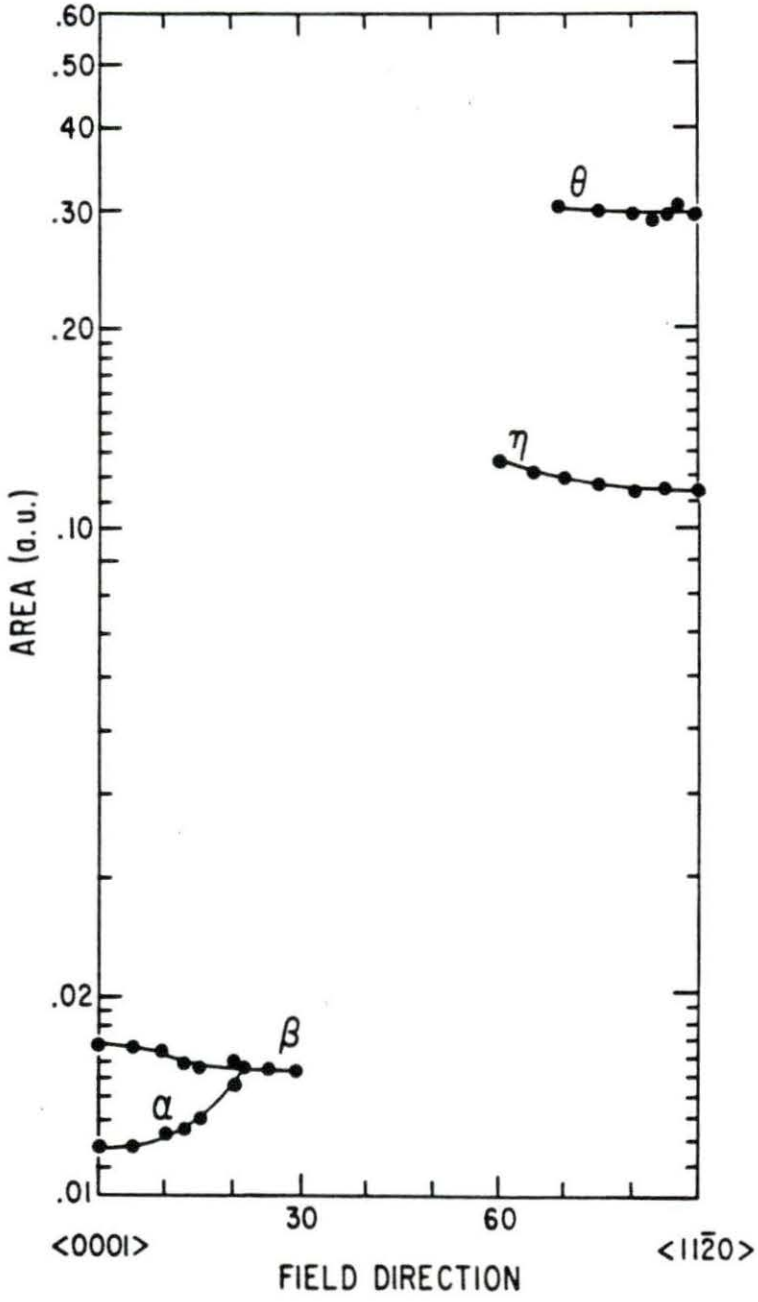

FIGURE 8. Experimental Angular Dependence of Orbits: 10$\bar{1}$0 Plane.

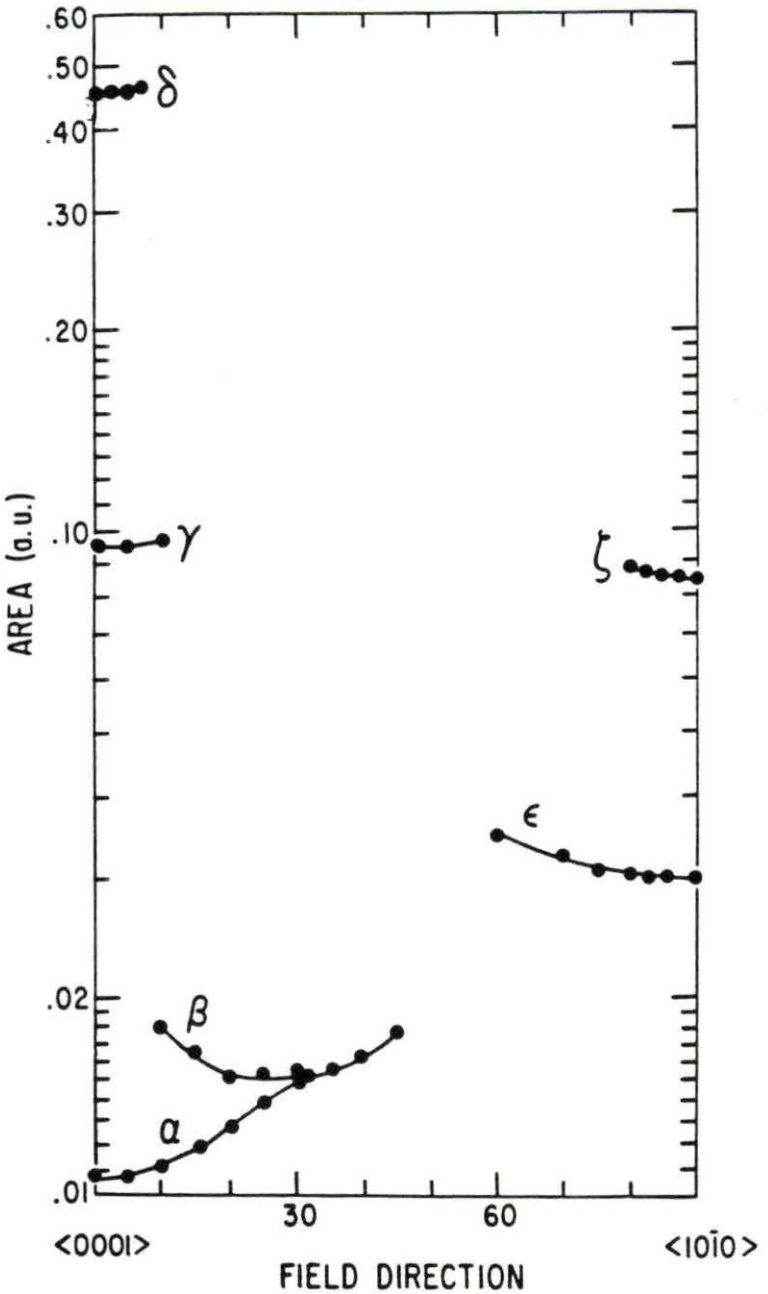

FIGURE 9. Experimental Angular Dependence of Orbits: 11$\bar{2}$0 Plane.

TABLE 1. Orbital Areas

ORBIT	AREA $(a.u.)^2$					
	EXP1	EXP2	POT1	POT2	POT(SR)	LOUCKS
α	.012	.010	.019	.023	*****	.021
β	.017	*****	.023	*****	*****	*****
β'	*****	*****	.036	.035	.028	*****
γ	.095	*****	.10	.11	.10	.10
δ	.45	*****	.43	.43	.42	.46
η	.114	*****	.097	.096	.099	.08
θ	.30	*****	.31	.31	.31	.34
ε	.030	*****	.048	.050	.053	.045
ζ	.085	*****	.094	.092	.09	.11

EXP1 : Experimental results of Johanson et al.
EXP2 : Experimental results of Hoekstra & Phillips.

given by the calculated band structure, as seen in Figures 11 and 12, although the magnitudes of the small orbits disagree. Note also the prediction of a β' orbit, which is unobserved experimentally, although yttrium[46], which is isoelectronic with lutetium and which exhibits a similar α-β type branching in the angular dependence of its dHvA frequencies, has an experimentally observed orbit corresponding to the predicted β' orbit. It should also be noted that a small shift in the Fermi level can make a substantial difference in the areas of the small orbits. In fact, a Fermi level shift of 5 mRy results in areas of .0144, .0154, and .0318 for the α, β, and β' orbits, which are more in line with the experimental areas.

We feel that the remaining disagreement between theoretical and experimental areas is mainly due to the MT approximation, rather than a

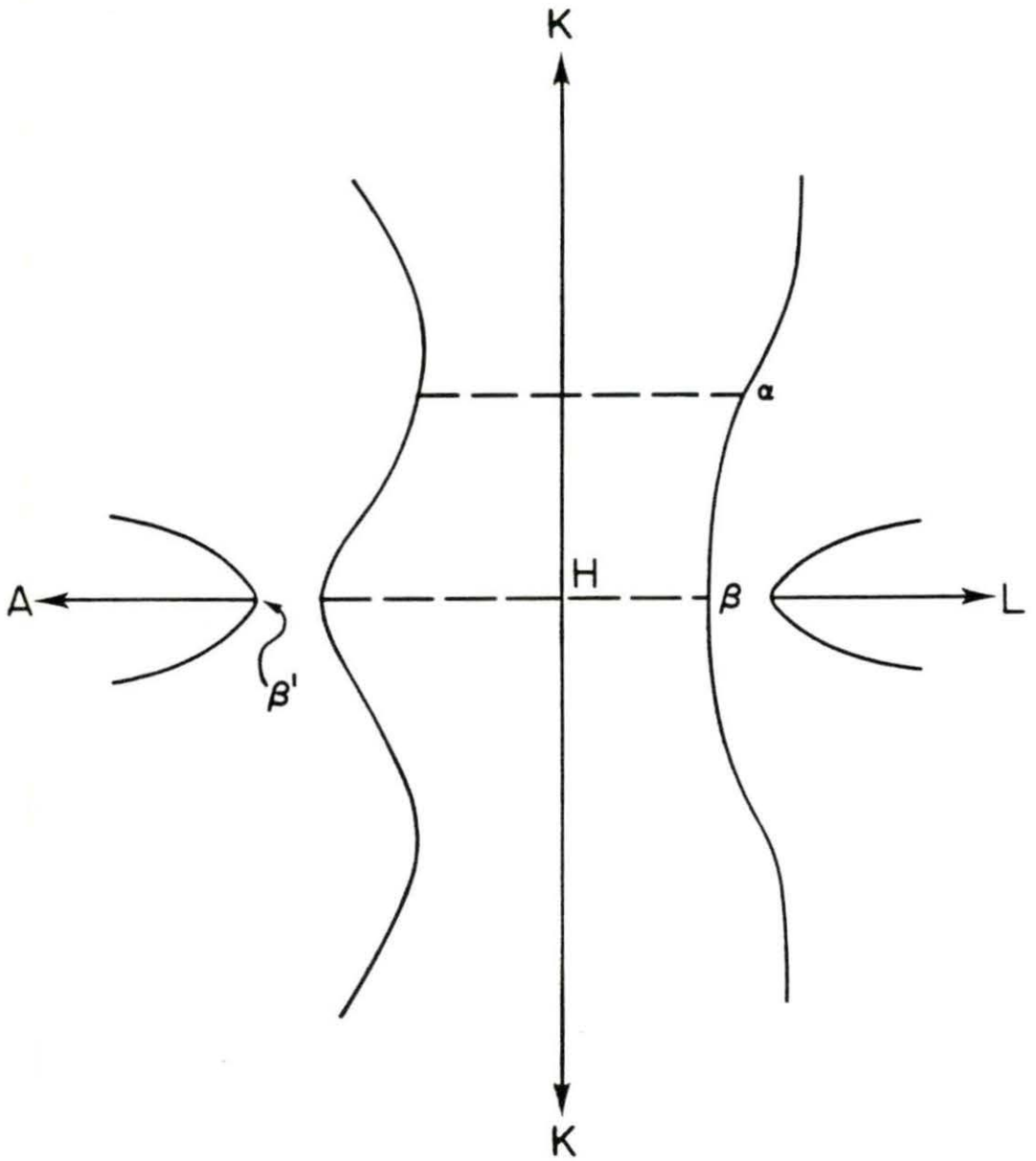

FIGURE 10. The α, β, and β-prime Orbits.

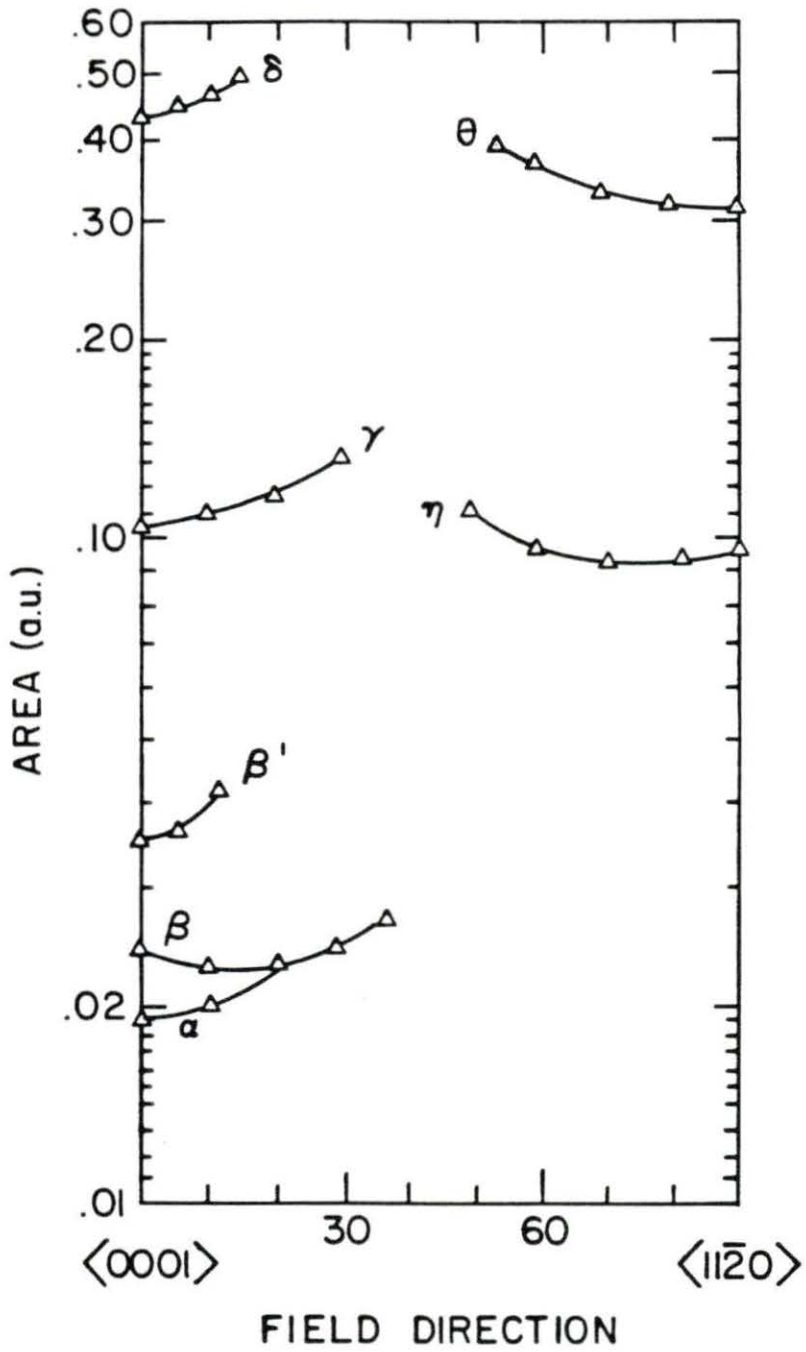

FIGURE 11. Theoretical Angular Dependence of the Orbits: 10$\bar{1}$0 Plane.

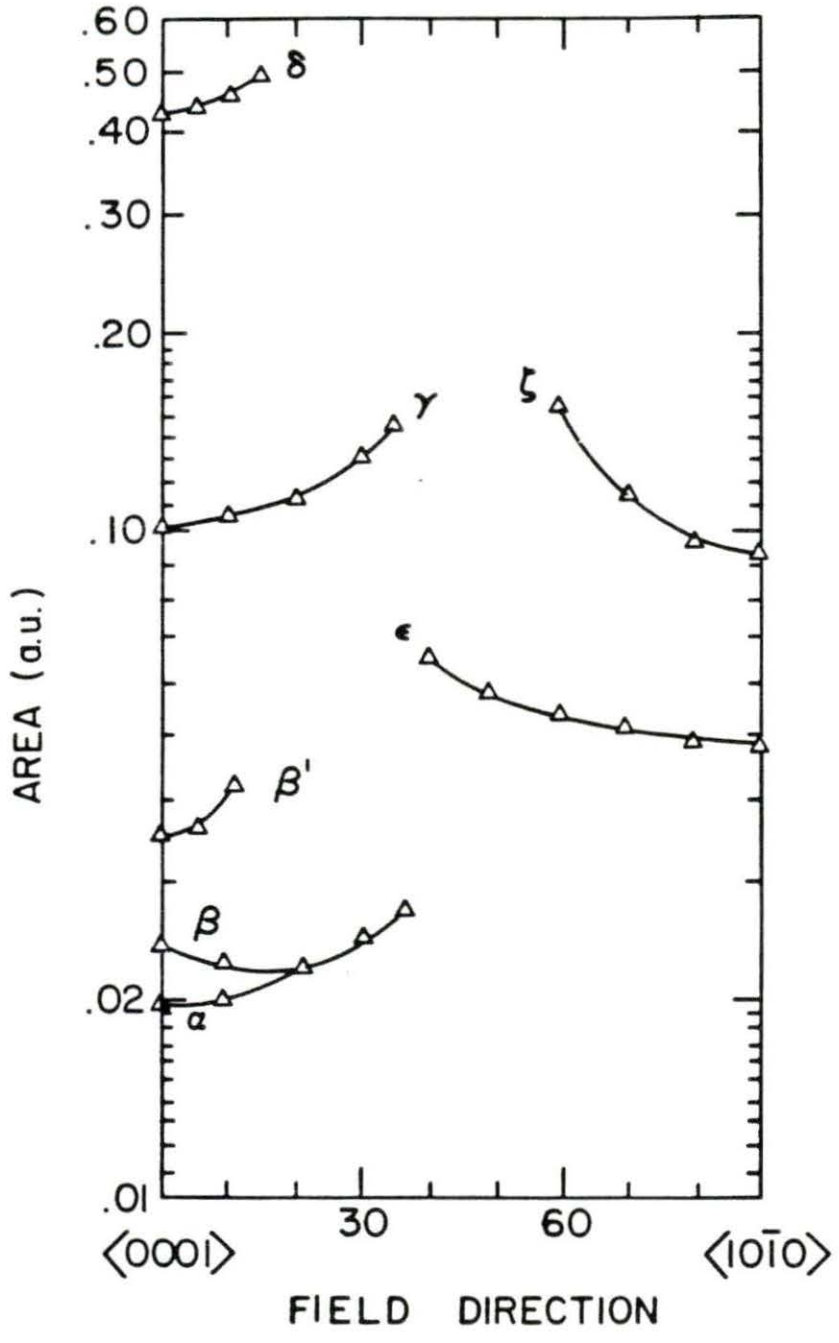

FIGURE 12. Theoretical Angular Dependence of the Orbits: 11$\bar{2}$0 Plane.

lack of self-consistency or poor placement of the f-bands. As a first approximation to the use of a more general potential, a warped (interstitial) potential from scandium was used for one additional iteration beginning with potential one, in place of the constant interstitial potential used in the MT approximation. This can be justified on the grounds that scandium is isoelectronic with lutetium, and the effort was made in order to see in which direction the inclusion of warping would move the energy bands. It was found that the resulting shift was in the correct direction, i.e., the Fermi surface was changed in such a way as to move the theoretical areas closer to the experimental areas.

Included in Table 2 are the experimentally observed and the calculated masses for the various orbits. The calculated masses are generally much smaller than the experimentally measured masses, suggesting a large electron-phonon mass enhancement, which is to be expected, as will be discussed in section four.

The Susceptibility

Another interesting feature of the Fermi surface of lutetium is the nesting of the two surfaces (i.e., the hole and electron sheets) due to the two bands which cross the Fermi level. Of particular interest is the "webbing" feature[19] seen in the LHMK plane, as shown in Figure 13, which is believed to determine the magnetic ordering wave vector Q in the heavy rare earth metals. For lutetium, Q was determined to be .53π/c by W.E. Evenson[47], who extrapolated the experimental results of W.C.

TABLE 2. Effective Masses

ORBIT	MASS(m*/mo)			
	EXP1	EXP2	POT1	POT2
α	.42	.38	.38	.42
β	.9	*****	.65	*****
β'	*****	*****	.74	.68
γ	*****	*****	-1.3	-1.3
δ	*****	*****	-3.9	-3.9
η	3.0	*****	1.7	1.7
θ	*****	*****	2.2	2.2
ε	1.7	*****	-.86	-.86
ζ	2.6	*****	-1.3	-1.3

EXP1 : Experimental results of Johansen et al.
EXP2 : Experimental results of Hoekstra & Phillips.

Koehler[3] for Tb-Lu alloys. Theoretically, the value of Q is determined from the maximum in the interband contribution to the suceptibility curve along the z direction, as shown in Figure 14. We take only the interband part because the webbing feature is caused by the interaction of the separate electron and hole surfaces due to the intersection of bands three and four with the Fermi level. The value found in this calculation is approximately 1.8 $a.u.^{-1}$ = .54π/c $a.u.^{-1}$. However, the shape and broadness of the peak are not understood, and possibly indicate the need for improved calculations, i.e., calculations in which the matrix elements are not assumed constant. Keeton and Loucks originally estimated Q to be about .45π/c from their band structure[19], but a later, more detailed calculation by Evenson and Liu[48], using the energy bands of Keeton and Loucks, gave a value of .54π/c . However,

Evenson and Liu used the root sampling method to perform their k-space integrals, resulting in a large scatter in their computed susceptibility curve, which could have introduced substantial uncertainty into their results.

The Specific Heat and Density of States

The theoretical density of states is shown in Figure 15. The value of the density of states at the Fermi level, N(Ef), is 23.54 States/Rydberg-Atom, which agrees with the result of 23.59 States/Rydberg-Atom obtained from the q = 0 limit of the susceptibility calculation. Taylor et al.[4], determined from specific heat measurements that the value of gamma, the coefficient of the low temperature linear term in the expression for the specific heat, is 8.3 ± .08 mJ/mole-deg K, or N(Ef) = 48.8 ± .5 States/Rydberg-Atom. Thome et al.[5], found gamma = 8.194 mJ/mole-deg K, implying that N(Ef) = 48.2 States/Rydberg-Atom, which is consistent with their purer sample.

Since this calculation ignores the electron-phonon interaction, it was expected that the calculated N(Ef) would be substantially lower than the measured gamma value. The difference is generally described in terms of an enhancement factor, λ , which is empirically given by:

$$N(Ef)exp = (1 + \lambda) N(Ef)theory$$

There are also contributions to the enhancement factor from the electron-electron interactions and from spin fluctuations. These contributions are generally assumed to be much smaller than the electron-phonon contribution, but recent theoretical[49] and

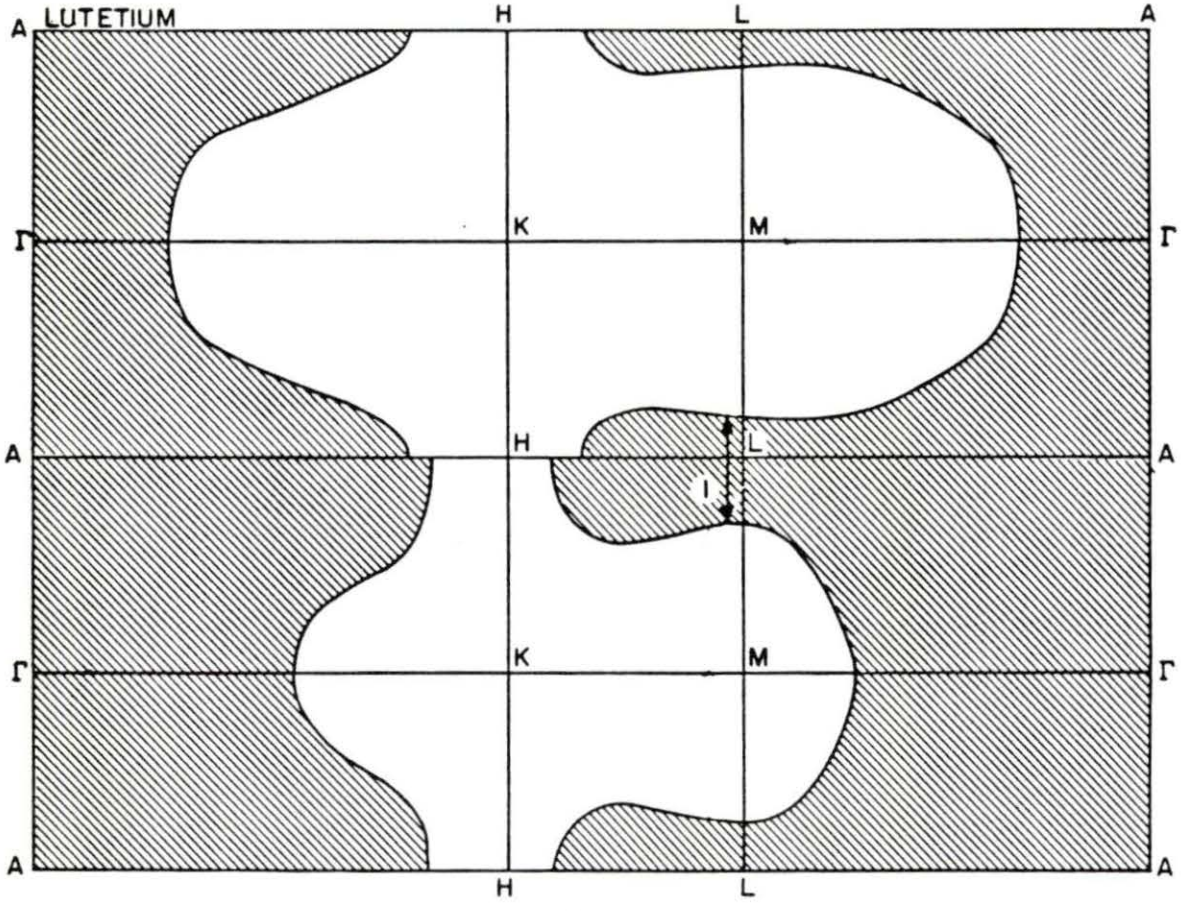

FIGURE 13. Webbing Feature in LHMK plane.

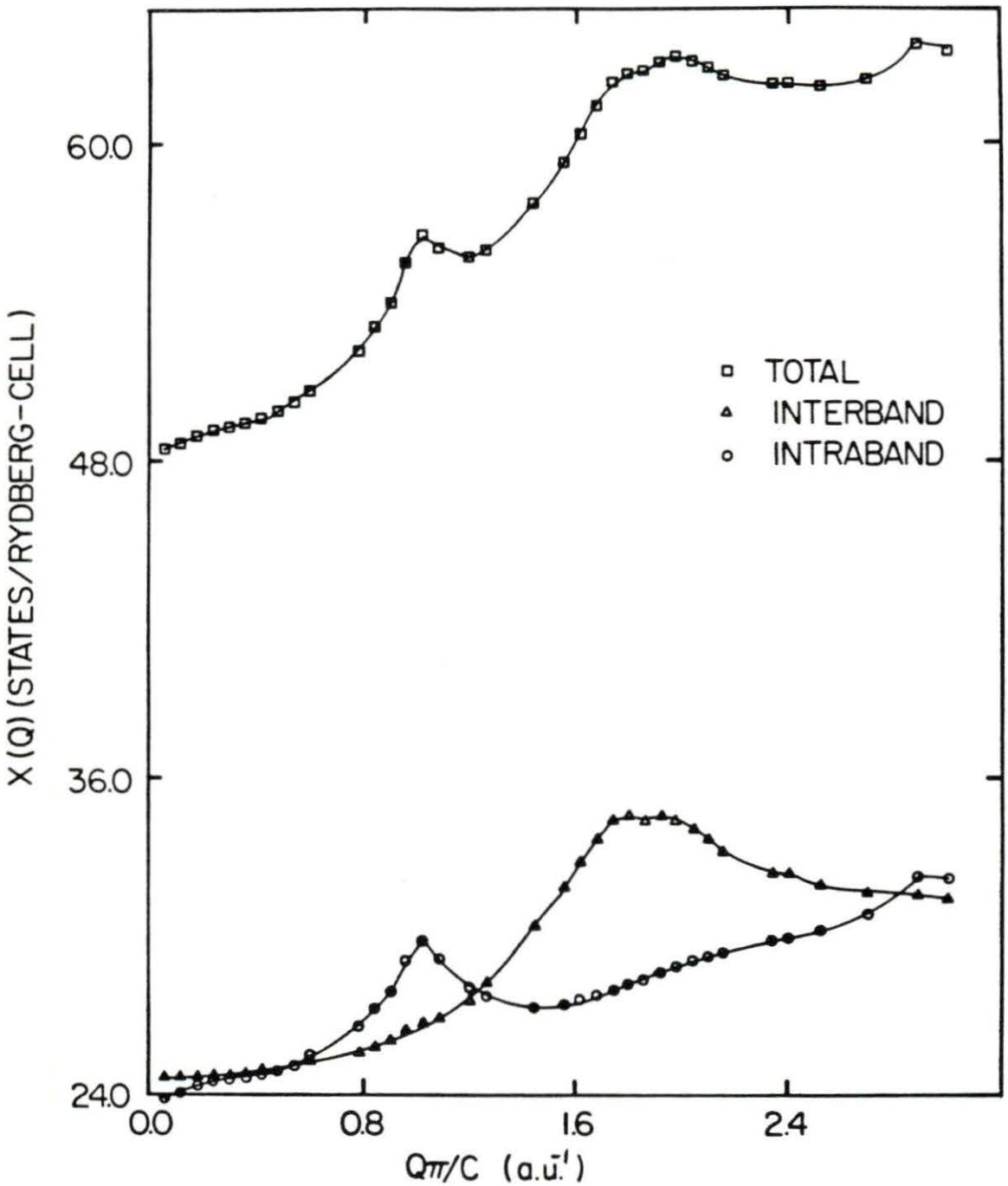

FIGURE 14. Theoretical Susceptibility Along z-axis.

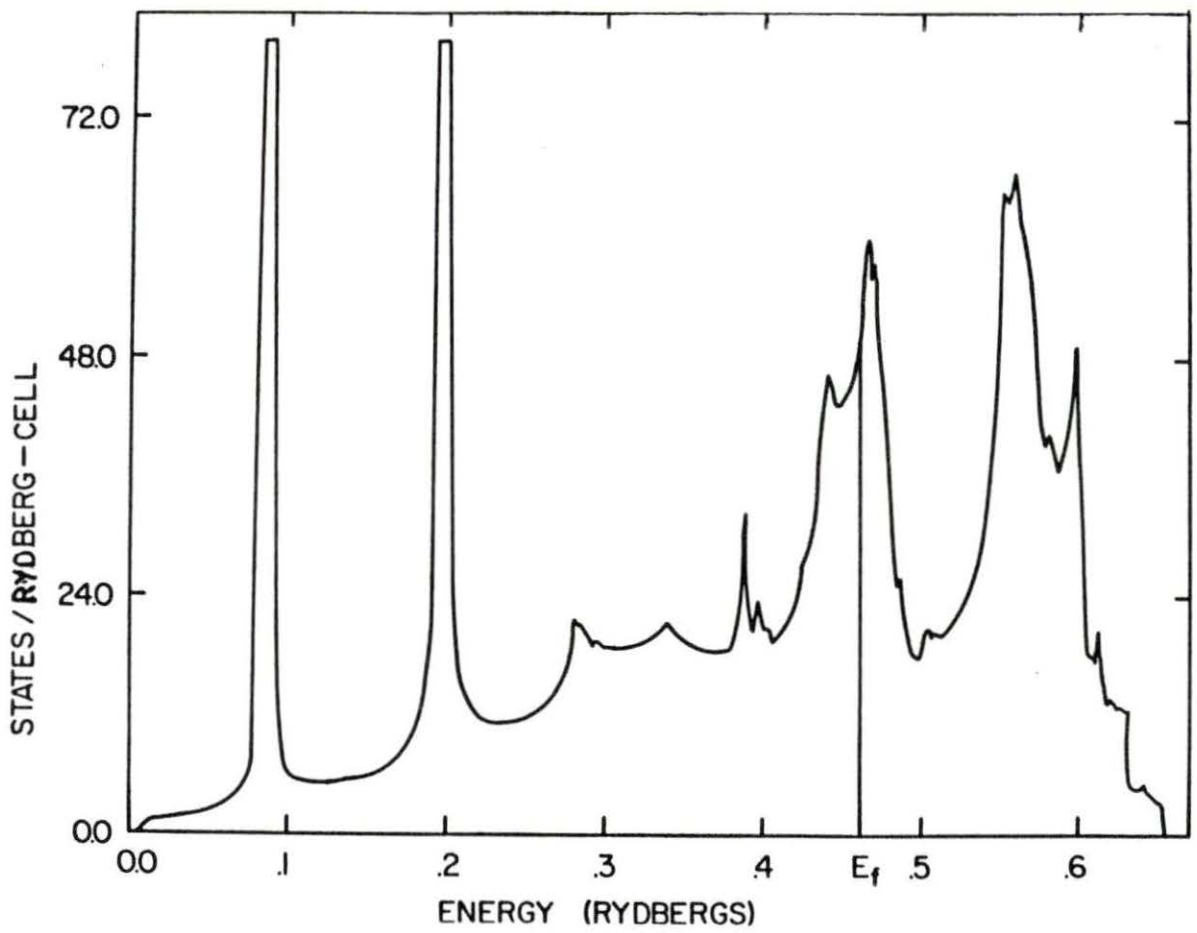

FIGURE 15. Theoretical Density of States.

experimental[50-51] work suggests that this may not be the case for transition and rare earth metals and their compounds. In general, the theoretical determination of λ is not yet very accurate, with estimates within about 25% of the correct values for transition metals[52-53]. More accurate calculations than this generally use quite a bit of experimental data in their calculations[15,54]. λ is measured by tunneling experiments for superconducting elements, and there is no λ value yet for lutetium. Values of 2. to .4 for the electron-phonon contribution have been reported for lutetium[55-56]. Our calculation, together with the data of Taylor et al., imply an empirical λ of 1.07, while the data of Thome et al., imply a λ of 1.05 for lutetium. Empirical results for the λ value of lutetium, as well as for scandium, yttrium, and lanthanum, which are isoelectronic with lutetium, as determined from the difference of experimentally measured gamma values and theoretically determined N(Ef) values, are compared with some experimental and theoretical results in Table 3. It should be observed that the results of this calculation are in line with those for the other materials, which are electronically similar.

As shown in the work of Thome et al., the addition of impurities such as hydrogen tended to increase the observed value of gamma until the hydrogen concentration reached 1.5 atomic percent, when the value of gamma started to decrease again. Thome et al. and Gschneidner et al.[64] suggest that this is due to the occurrence of hydrogen tunneling between equivalent interstitial sites in the presence of oxygen. The effect of this tunneling is to contribute a low temperature linear term to the

TABLE 3. Enhancement Factors

MATERIAL	LAMBDA	REFERENCES
Lu	1.05 --> 1.07	(a)
	.89 --> .91	(b)
La	1.15	(c)
	1.4	(c)
	.77 --> .84	(d)
Y	.74	(e)
	1.15	(f)
	.28 --> .38	(g)
	.55 --> .67	(c)
Sc	.98	(f)
	1.25	(h)
	.49 --> .64	(g)
	.81	(c)

(a) Results of this calculation compared with ref. 4 & 5.
(b) Results of ref. 19 compared with ref. 4 & 5.
(c) Results of ref. 54 assuming fcc or bcc structure.
(d) Experimental results of refs. 57 & 58.
(e) Results of ref. 59 compared with ref. 4 .
(f) Results of ref. 60 compared with ref. 61.
(g) Results of ref. 52.
(h) Results of ref. 49 compared with ref. 62.

specific heat. This explanation is more reasonable than interpreting the desity of states in a rigid band manner, which would suggest that the hydrogen added electrons, causing the Fermi level to move upward, thus increasing N(Ef). However, the addition of hydrogen may not add electrons. In fact, the interstitial impurities probably reduce the electron concentration, due to the electronegative nature of the impurities relative to the electropositive nature of lutetium.

Furthermore, it should be noted that in the the case of LaH2, YH2, and ScH2, charge tended to be transferred to the hydrogen[63], although one should not arbitrarily extrapolate results for dihydrides to systems which are essentially pure metals with small amounts of hydrogen impurities. Several earlier specific heat measurements, referenced by Thome et al, which involved less pure samples of lutetium, produced much higher gamma values, in line with the results of Thome et al.

This electron-phonon enhancement factor also applies to band masses which are calculated while ignoring the electron-phonon interaction. As can be seen in Table 2, an enhancement on the order of 1.0 would bring the theoretical masses of the larger orbits more in line with the experimentally observed masses.

The Magnetic Form Factor

The wavefunctions produced in a band structure calculation are much more sensitive to small changes in the potential than are the energy bands. For that reason, the magnetic form factor is a good test of the theoretical results. The results of a neutron magnetic form factor measurement by Stassis et al., are shown in Figure 16, along with their calculated spin and orbital atomic form factors and non-self-consistent RAPW spin form factor[6]. The experimental results presented here have already had the diamagnetic contribution, as calculated by the Stassis diamagnetic form factor[65], subtracted out. It should be noted that the atomic form factor does not agree with experiment, unlike the case with the transition metals located toward the right side of the periodic

table. This can be understood in light of the fact that, for paramagnetic systems, the form factor reflects the character of the wavefunctions at the Fermi level. As shown in Figure 17, for a Fermi energy near the bottom of the d-bands, one has a bonding type state, with a charge density which is spread out towards the nearest neighbors, and is much more expanded than in the atomic case. As one progressively fills the d shell, the Fermi level moves upward toward the antibonding type states at the top of the d-bands, which have much more contracted charge densities and are hence much more atomic-like. Thus, solids with nearly filled d-bands should have form factors which can be fairly closely approximated by the atomic results.

It should be noted that the measured form factor of Stassis et al. falls off more rapidly than the atomic form factor, which agrees with expectations due to the expanded d wavefunctions and the large amount of s-p type character at the Fermi level. The results of the spin-only RAPW calculation of Stassis et al., are in extremely good agreement with experiment, implying that there is no significant orbital contribution. However, anisotropy in the susceptibility measurement[66] suggests that there should be a large orbital contribution, possibly on the order of 40-60%. This discrepancy was part of the motivation for this self-consistent calculation. The results of this calculation are also shown in Figure 16, and are in almost as good agreement with experiment as the RAPW results. The results of this calculation, using Hedin-Lundqvist exchange, are lower than the α=1 RAPW results at the first few reflections. However, at the higher reflections, it appears that the

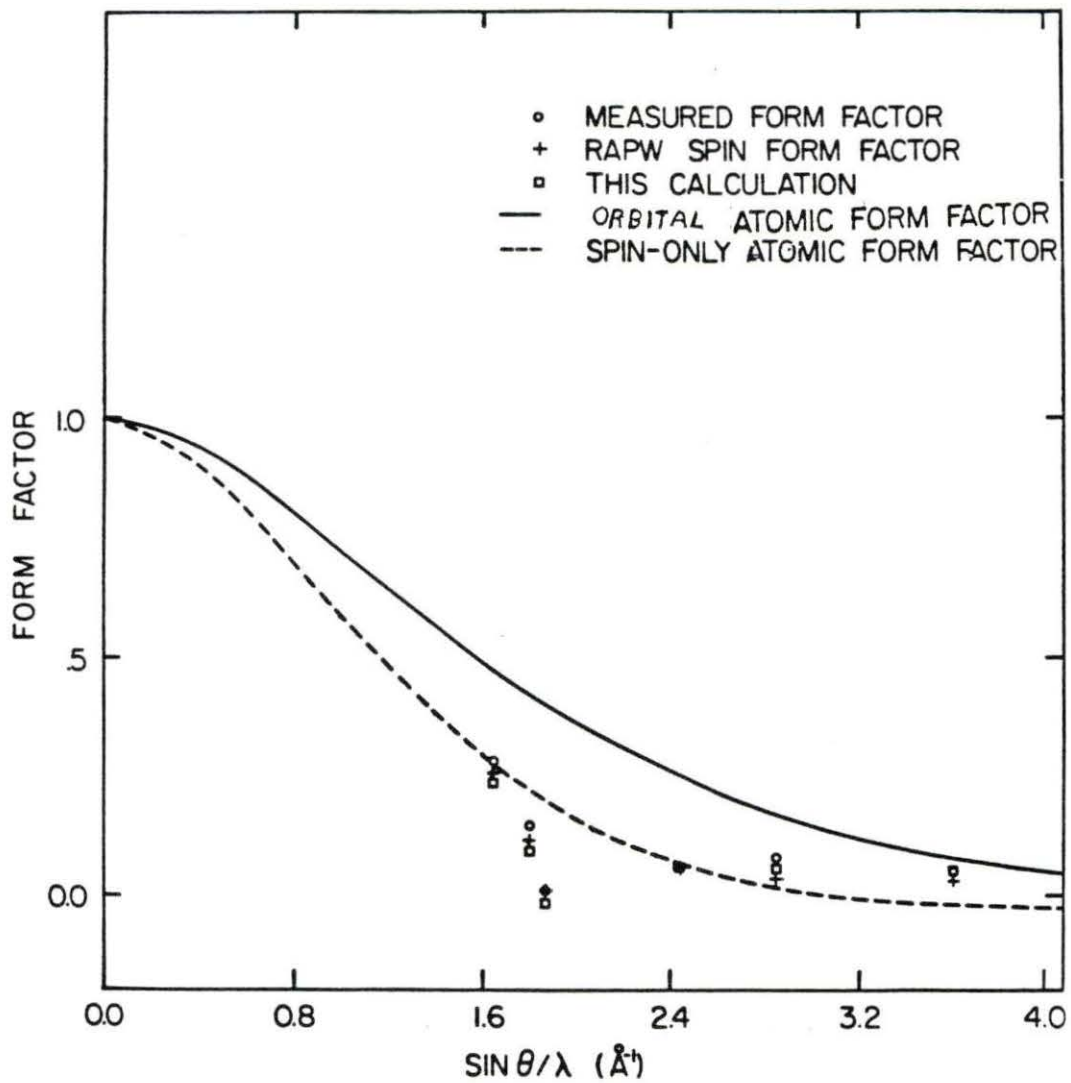

FIGURE 16. The Induced Neutron Magnetic Form Factor.

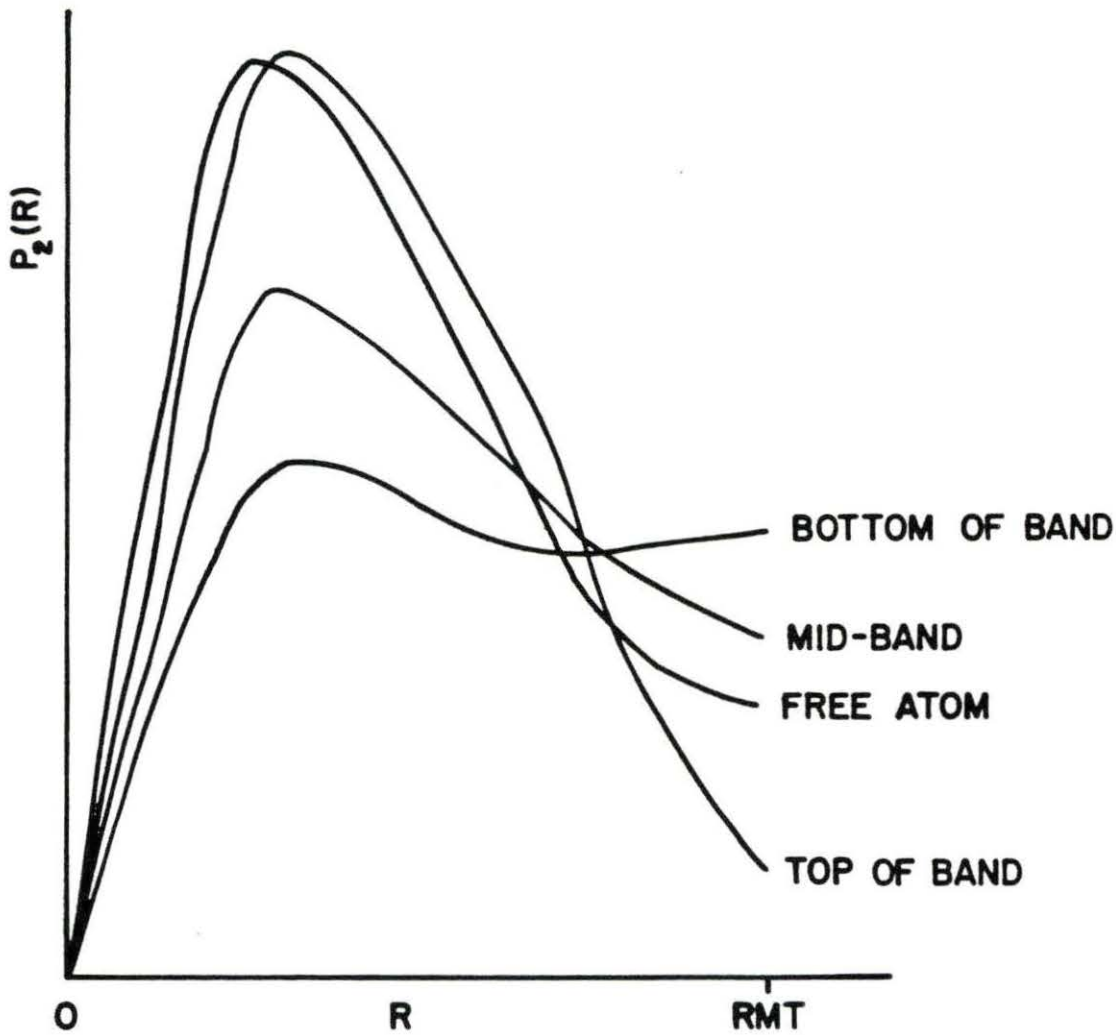

FIGURE 17. Energy Dependence of the Radial d Wavefunctions.

anisotropy observed in the susceptibility measurements starts to come into play. The main cause of this anisotropy is the asphericity of the spin density. It has been suggested by Gupta and Freeman[67-68], that, in the case of scandium, another cause is interference, through the Fourier transform, of the inner and outer parts of the magnetization density. However, we have not found this to be a contributing factor in the case of lutetium. Since the asphericity is so sensitive to the potential, the MT approximation may be responsible for the theoretical results becoming larger than the experimental results at higher reflections.

We calculated the unenhanced Pauli spin susceptibility, which is given in terms of the density of states at the Fermi level by μ_β^2 N(Ef), and came up with a value of 56×10^{-6} emu/mole. The total susceptibility, as determined by Spedding and Croat, is 189×10^{-6} emu/mole, which suggests that the ratio of orbital to spin contributions should be roughly two to one, implying a gyromagnetic ratio of about 1.2. Unfortunately, the gyromagnetic ratio has not been measured for lutetium, as it could be in principle by an Einstein-de Haas experiment. Although a large exchange enhancement could decrease the required orbital contribution, as in scandium, it is not believed that there will be an exchange enhancement much bigger than 2.0 in lutetium. The reason for this is the general trend observed as one goes from the 3d to the 4d to the 5d elements, in which the spatial extent of the d-orbitals increases. As the orbitals become more extended, less exchange enhancement is observed. This is evident from the work of Moruzzi et al.[31], which only dealt with elements through atomic number 49, but

which illustrated the trend. They found theoretically that the enhancement of scandium, a 3d metal, was about 40 percent larger than for yttrium, a 4d metal. Since both scandium and yttrium are isoelectronic with lutetium, this should be indicative of the trend.

The calculation of the form factor involves an expansion of the charge density inside each MT sphere in terms of a series of lattice harmonics, which are constructed with the symmetry of the lattice. Each expansion term is characterized by its angular momentum quantum numbers, L and M. The charge density can be broken down into these different L and M contributions, which is often helpful in illustrating the physics. In Figure 18, the various LM contributions to the charge density inside the MT sphere are graphically represented. The spherically symmetric (L=0,M=0) part dominates, with the aspherical L=3 component contributing most of the remainder of the charge density. This L=3 component is mainly from the interaction of the d(50-70 %) and the p(25-35%) bands, as there is very little f character present in the wavefunctions at the Fermi level. The large amount of p-type charge is evident from the sharp rise in the spherical density at the MT radius. Since the Fermi level is near the bottom of the d-bands, one would expect the d-only contribution to have the appearance of the bonding type orbital, as shown in Figure 17.

In Table 4, the various theoretical and experimental form factors are tabulated. The column labeled spherical contains the form factor which results if only the spherical part of the charge density inside the MT is included, but including the aspherical components from the

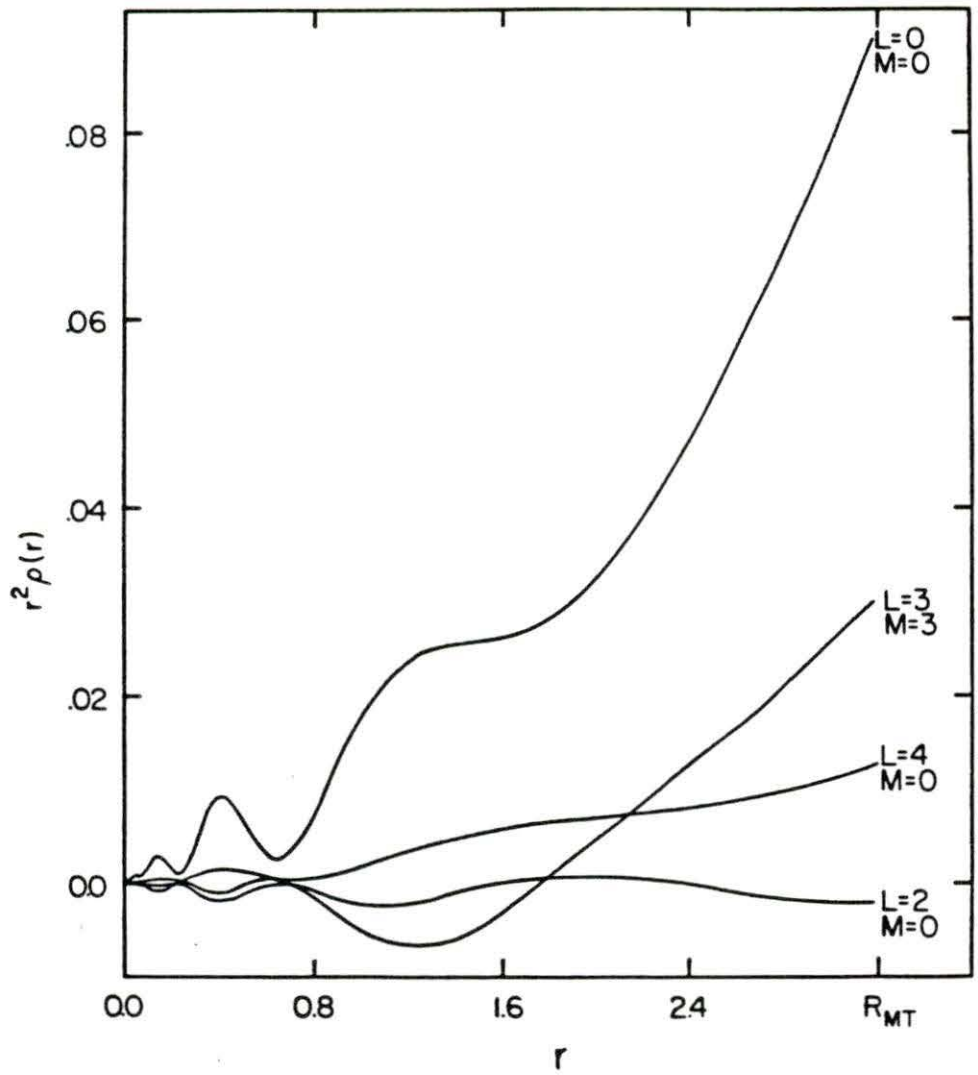

FIGURE 18. Angular Momentum Decomposition of the Charge Density.

interstitial region. It can be seen that a substantial part of the form factor is due to nonspherical terms, and that the assumption of spherical symmetry inherent in the MT approximation probably has a detrimental effect on the results. Additionally, it has been found that the wavefunctions and form factor are sensitive to the interstitial potential in the rare earths[36], suggesting that WMT effects could modify the form factor results.

TABLE 4. The Neutron Magnetic Form Factor

$\frac{\sin(\theta)}{\lambda}$	FORM FACTOR					
	EXP	RAPW	THIS CALC.	SPIN ATOMIC	ORBIT. ATOMIC	SPHER.
0.0				1.00	1.00	
0.1648	.278	.254	.235	.28	.48	.16
0.1801	.145	.114	.094	.23	.43	.072
0.1870	.006	.013	-.017	.21	.41	.01
0.244	.057	.064	.061	.068	.25	.035
0.285	.079	.036	.056	.017	.17	.040
0.360	.044	.028	.049	-.022	.08	.004

DISCUSSION AND CONCLUSIONS

This investigation has shown that the SO-LAPW method, within the limitations of the local density (Hedin-Lundqvist) and MT approximations, is capable of producing a fully relativistic bandstructure and associated electronic properties of hcp lutetium which are in good agreement with experimental results, while requiring less computational effort than an RAPW calculation. It has been found that, for lutetium, the absolute placement of the 4f-bands is not as important as previously thought, insofar as energy-band related properties are concerned. Although the 4f placement is extremely sensitive to the actual potential used, the actual shape and size of the Fermi surface were not appreciably changed by the movement of the 4f-bands within a fairly wide region. Furthermore, it is felt that the majority of the charge error still existing after the last iteration was due to the "bouncing around" of the 4f-levels, and that, in fact, a good approximation of self-consistency had been reached. The angular dependence of the theoretical dHvA orbits was in good agreement with experiment, demonstrating that the shape of the theoretical Fermi surface was in good agreement with the experimental Fermi surface. The main discrepancy between theoretical and experimental results was in the areas of the small orbits, which are very sensitive to small changes in the Fermi surface. It is felt that it will be necessary to use a more general potential to bring the small orbital areas into line with experiment. Furthermore, it is not believed that a better exchange-correlation potential will have as much of an effect on the Fermi

surface of lutetium as will an improvement on the MT approximation. A better exchange-correlation potential, perhaps along the lines of the Self-Interaction-Corrected Average Density Approximation (SIC-ADA) formulation of density-functional theory[32], will be necessary to treat the 4f-bands realistically, especially in other rare earth metals with open 4f-shells. A better treatment of exchange and correlation will probably be required for the generation of accurate wavefunctions. Furthermore, since the Fermi energy is near the bottom of the d-bands, the error in the placement of the d-bands, due to the inaccuracies of the LDA, should not be very large.

This magnetic form factor calculation, using Hedin-Lundqvist exchange-correlation and with some degree of self-consistency, showed anomalously good agreement with experiment in light of the expected large orbital contribution, which was neglected. With the expected 40-60% orbital contribution, as estimated from from the susceptibility measurements and the atomic calculations, the spin only form factor should have disagreed substantially with experiment. Possibly, the exchange enhancement is larger than expected. We have shown that the surprisingly good agreement with experiment obtained by Stassis et al., was not entirely due to their use of wavefunctions from a non-self-consistent calculation. It appears that it will be necessary to perform the calculation with a more general potential, due to the large aspherical contributions, which are sensitive to the interstitial potential. In any event, an actual calculation of the orbital contribution to the form factor, along the lines of the Oh et al.

calculation for chromium[43], would be extremely helpful in assessing the actual orbital contribution in the solid. In addition, Einstein-de Haas experiments to measure the gyromagnetic ratio would shed some light on the actual breakdown of the spin and orbital contributions to the form factor.

APPENDIX : CALCULATIONAL DETAILS

Lutetium occurs in the hcp structure with symmetry group D6h. It has an atomic number of 71, with a valence of $5d^1 6s^2 4f^{14}$, and two atoms per unit cell. We have used experimentally determined lattice constants[69] of a=b= 6.61990 a.u. and c= 10.48968 a.u., which produce a unit cell volume of 398.10 $(a.u.)^3$. Since we are working within the APW framework, we must decide how large to make the MT spheres around each ion. Generally, in the homonuclear case, where both spheres are taken to be the same size, one makes them as large as possible without overlapping. We chose an MT radius of 3.17988 a.u., which results in a sphere volume of 134.6855 $(a.u.)^3$. Thus, 67.7% of the cell volume is within the two spheres. We use a standard logarithmic mesh for calculational purposes, which makes the spacing between mesh points smaller in the inner regions of each sphere, where the charge density is varying more rapidly. For a given mesh point I, the radius is given by:

$$R(I) = RN * EXP[(I-1) * DX]$$

where: $RN = RNOT * EXP[(I-R1) * DX] = .00011968$ a.u.

$DX = 1/32 = .03125$

$R1 = 421$

$RNOT = 60$

The MT radius (RMT) is defined in terms of a mesh point JRI, i.e., RMT=R(JRI). In this case, JRI = 327, which gives the previously mentioned value for RMT. We further define RKM, which limits the number of reciprocal lattice vectors, i.e., basis functions to be included in the sums. Only those vectors are included, which, at each k-point,

satisfy:

$$| \underline{k} + \underline{K} | < RKM/RMT$$

We use a value of RKM = 7, which generally results in 70-80 basis vectors, and a convergence of approximately 1 mRy for the one-electron eigenvalues. In the sums over angular momentum states, we include terms up to l=12, which provides good convergence.

Due to the high symmetry of the hcp unit cell, we can perform our calculations within an irreducible wedge of the cell, which is 1/24 of the entire cell volume, as shown in Figure 19. The rest of the cell can be reproduced by the symmetry operations of the lattice. We used 27 k-points within the irreducible wedge for our iterations, which were chosen by dividing the irreducible wedge into 27 smaller wedges, and then taking the k-point at the center of mass of each wedge. Each k-point was equally weighted in the calculations. An earlier test consisted of a series of iterations using 64 k-points, both with and without strengthened exchange, which did not noticeably change convergence or improve the 4f situation.

During the 27 point iterations towards self-consistency, we used an overall energy parameter of .4 Rydbergs. We set the l=1 energy parameter at 1.2 Rydbergs to prevent the generation of spurious 6p-bands which could influence the 4f-bands. The l=3 parameter had to be adjusted very carefully to the center of the f-bands for each iteration. Since the 4f's had a bandwidth of less than 10 mRy, it was necessary to check the change in 4f position each time for a few k-points and then adjust the new l=3 energy before continuing the iterations. During the

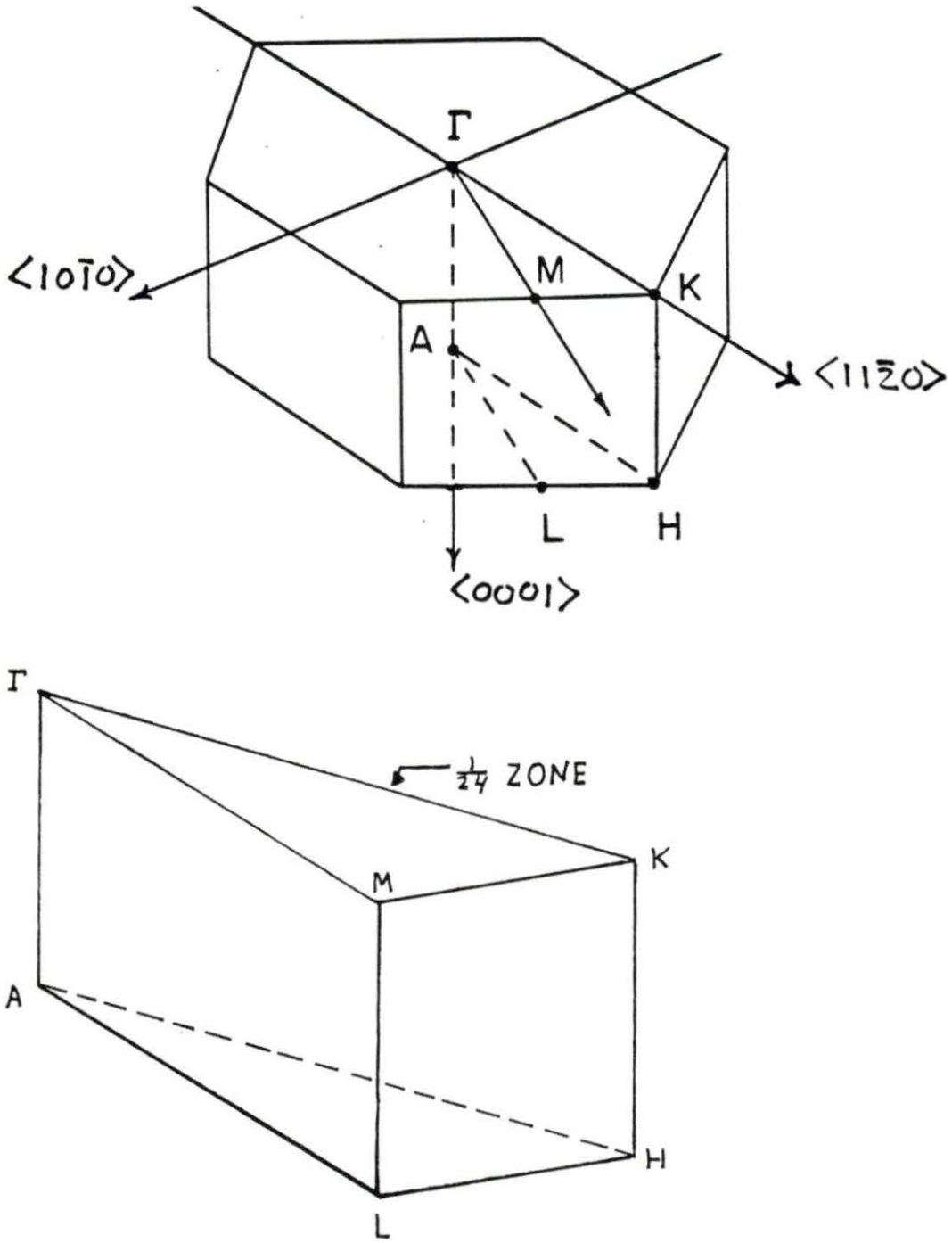

FIGURE 19. One half hcp Unit Cell and Irreducible Wedge

iterations, charge tended to move from the interstitial regions into the spheres. During the final iteration, the charge within each sphere was 70.0150 electrons.

Once we had arrived at our final potential, our final iteration consisted of using 142 k-points both inside the wedge and along high symmetry lines. This final iteration included spin-orbit coupling, and the resultant 20 eigenvalues per k-point were fit using a 60 function Fourier series consisting of symmetrized plane waves, with each band fit separately. The RMS fitting fitting error was less than 2 mRy for the two bands which define the Fermi surface and was generally less than 1 mRy for the remaining bands. The bands shown in Figure 1 were generated using these coefficients. As can be seen in that Figure, there is a splitting of the bands along the LA direction, where, by symmetry, the bands should be degenerate. This is caused by an inadequacy in the Fourier series fit. These fitting coefficients were then used to produce a high resolution density of states via the tetrahedron method, as well as the band structure along high symmetry lines. The coefficients were also used in our orbit tracing program to produce the orbits and angular dependencies shown earlier. The orbit tracing routine was tested on a cylindrical Fermi surface and was found accurate to at least 4 decimal places, which is probably more accurate than our convergence and fitting errors warrant. The bands generated by the Fourier series fit generally matched the bands from the first principle calculation well, except around the H point. It was necessary to generate 282 first principle points in the region around the H point and

perform another 60 function fit in order to correctly bring out the details of the Fermi surface in that area.

The susceptibility curve was generated by the constant matrix element tetrahedron method mentioned earlier, using 1536 small tetrahedra within the irreducible wedge. This number of small tetrahedra is quite sufficient, as the agreement of the q=0 limit with the density of states illustrates. Most of the error in the calculation will be due to the assumption of constant matrix elements.

The form factor was calculated as follows. First, the irreducible zone was divided into 1536 small tetrahedra. Then, k-points were generated for each tetrahedron which contained a piece of the Fermi surface, along with an appropriate weight, given by the area of the small piece of the Fermi surface divided by the gradient of the energy. The resultant 680 k-points were used to generate wavefunctions at the Fermi level using the SO-LAPW method. However, due to inaccuracies in the Fourier series fit, etc., only 561 wavefunctions, which had corresponding eigenvalues within 15 mRy of the Fermi energy were used. These wavefunctions were then summed with the correct weights to produce a charge density, which was then used to produce the final spin only form factor.

REFERENCES

1. A. H. MacDonald, W. E. Pickett, and D. D. Koelling, J. Phys. C: Sol. State Phys., 13, 2675 (1980).

2. W. R. Johansen, G. W. Crabtree, and F. A. Schmidt, J. Appl. Phys., 53, 2041 (1982).

3. W. C. Koehler, J. Appl. Phys., 36, 1078 (1965).

4. W. A. Taylor, M. B. Levy, and F. H. Spedding, J. Phys. F: Metal Phys., 8, 2293 (1978).

5. D. K. Thome, K. A. Gschneidner, Jr., G. S. Mowry, and J. F. Smith, Sol. St. Comm., 25, 297 (1978).

6. C. Stassis, G. R. Kline, C.-K. Loong, and B. N. Harmon, Sol. St. Comm., 23, 159 (1977).

7. J. O. Dimmock and A. J. Freeman, Phys. Rev. Lett., 13, 750 (1964).

8. A. J. Freeman, in Magnetic Properties of Rare Earth Metals, edited by R.J. Elliot (Plenum Press, New York, 1972), p. 245.

9. B. Y. Tong and L. J. Sham, Phys. Rev., 144, 1 (1966).

10. B. N. Harmon and A. J. Freeman, Phys. Rev., B10, 1979 (1974).

11. R. C. Young and J. F. Hulbert, Phys. Lett., 47A, 367 (1974).

12. J. E. Schirber, F. A. Schmidt, B. N. Harmon, and D. D. Koelling, Phys. Rev. Lett., 36, 448 (1976).

13. R. C. Young, R. G. Jordan, and D. W. Jones, Phys. Rev. Lett., 31, 1473 (1973).

14. Allan H. MacDonald, Ph.D. thesis, unpublished, University of Toronto, Toronto, Ontario, Canada, 1978.

15. Warren E. Pickett , A. J. Freeman, and D. D. Koelling, Phys. Rev., B22, 2695 (1980).

16. J. C. Slater, Phys. Rev., 51, 846 (1937).

17. T. L. Loucks, Phys. Rev., 139, a1333 (1965).

18. S. C. Keeton and T. L. Loucks, Phys. Rev., 146, 429 (1966).

19. S. C. Keeton and T. L. Loucks, Phys. Rev., 168, 672 (1968).

20. J. C. Slater and H. M. Kruttner, Phys. Rev., 47, 559 (1935).

21. O. Krogh Andersen, Phys. Rev., B12, 3060 (1975).

22. D. D. Koelling and G. O. Arbman, J. Phys. F: Metal Phys., 5, 2041 (1975).

23. O. K. Andersen, Sol. St. Comm., 13, 133 (1973).

24. D. D. Koelling and B. N. Harmon, J. Phys. C: Sol. St. Phys., 10, 3107 (1977).

25. J. C. Slater, Phys. Rev., 81, 385 (1951).

26. R. Gaspar, Acta Phys. Acad. Sci. Hung., 3, 263 (1954).

27. W. Kohn and L. J. Sham, Phys. Rev., 140, A1133 (1965).

28. J. C. Slater and K. H. Johnson, Phys. Rev., B5, 844 (1972), and references therein.

29. L. Hedin and B. I. Lundqvist, J. Phys. C: Sol. State Phys., 4, 2064 (1971).

30. P. Hohenberg and W. Kohn, Phys. Rev., 136, B864 (1964).

31. V. L. Moruzzi, J. F. Janak, and A. R. Williams, Calculated Electronic Properties of Metals (Pergammon, New York, 1978).

32. L. A. Cole and B. N. Harmon, J. Appl. Phys., 52, 2149 (1981), and references therein.

33. D. D. Koelling, A. J. Freeman, and F. M. Mueller, Phys. Rev., B1, 1318 (1970).

34. P. D. DeCicco, Phys. Rev., 153, 931 (1967).

35. D. D. Koelling, Phys. Rev., 188, 1049 (1969).

36. B. N. Harmon, Ph.D. thesis, unpublished, Northwestern University, Evanston, Illinois, 1973.

37. A. R. Williams and J. Morya, J. Phys. C, 7, 37 (1974).

38. Naim Elyashar, Ph.D. thesis, unpublished, University of Illinois, Chicago, Illinois, 1975.

39. L. Kleinman and R. Shurtleff, Phys. Rev., 188, 1111 (1969).

40. L. Kleinman and R. Shurtleff, Phys. Rev., B4, 3284 (1971).

41. Ryogo Kubo, J. Appl. Phys., 36, 1078 (1957).

42. J. Rath and A. J. Freeman, Phys. Rev., B11, 2109 (1975).

43. K. H. Oh, B. N. Harmon, S. H. Liu, and S. K. Sinha, Phys. Rev., B14, 1283 (1976).

44. Steven P. Kowalczyk, Ph.D. thesis, unpublished, Lawrence Berkeley Lab Report Number 4319, 1976.

45. J. A. Hoekstra and R. A. Phillips, Phys. Rev., A4, 4184 (1971).

46. P. G. Mattocks and R. C. Young, J. Phys. F: Metal Phys., 8, 1417 (1978).

47. W. E. Evenson Ph.D. thesis, unpublished, Iowa State University, Ames, Iowa, 1968.

48. W. E. Evenson and S. H. Liu, Phys. Rev. Lett., 21, 482 (1968).

49. Shashikala G. Das, Phys. Rev., B13, 3978 (1976).

50. K. Ikeda and K. A. Gschneidner, Jr., Phys. Rev. Lett., 45, 1341 (1980).

51. G. W. Crabtree, D. H. Dye, D. P. Karim, D. D. Koelling, and J. B. Ketterson, Phys. Rev. Lett., 42, 390 (1979).

52. D. A. Papaconstantopoulos, L. C. Boyer, B. M. Klein, A. R. Williams, V. L. Moruzzi, and J. F. Janak, Phys. Rev., B15, 4221 (1977).

53. R. Evans, G. D. Gaspari, and B. L. Gyorffy, J. Phys. F: Metal Phys., 3, 39 (1973).

54. Warren E. Pickett, Physica, 111B, 1 (1981).

55. K. H. Bennemann, and J. W. Garland, in Superconductivity in d- and f-band Metals-1971, edited by D.H. Douglas, AIP Conference Proceedings Number 4, 103 (1971).

56. J. J. Hopfield, Physica, 55, 41 (1971).

57. H. Wuehl, A. Eichler, and J. Wittig, Phys. Rev. Lett., 31, 1393 (1973).

58. L. F. Lou, and W. J. Tomasch, Phys. Rev. Lett., 29, 858 (1972).

59. T. L. Loucks, Phys. Rev., 144, 504 (1966).

60. G. S. Fleming, and T. L. Loucks, Phys. Rev., 173, 685 (1968).

61. S. L. Altmann, and C. J. Bradley, Proc. Phys. Soc. (London), 92, 764 (1967).

62. G. S. Knapp, and R. W. Jones, Phys. Rev., B6, 176 (1972).

63. D. J. Peterman and B. N. Harmon, Phys. Rev., B20, 5313 (1979), and references therein.

64. Karl A. Gschneidner, Jr., H. Gnugesser, and K. Neumaier, Physica, 108B, 1007 (1981).

65. C. Stassis, Phys. Rev. Lett., 24, 1415 (1970).

66. F. H. Spedding and J. J. Croat, J. Chem. Phys., 59, 2451 (1973).

67. Raju P. Gupta and A. J. Freeman, Phys. Rev. Lett., 36, 613 (1976).

68. A. J. Freeman, Proc. of the Conference on Neutron Scattering, 2, 592 (1976).

69. W. B. Pearson, A Handbook of Lattice Spacings and Structures of Alloys (Pergammon, New York, 1958).

ACKNOWLEDGEMENTS

I would like to thank Dr. Bruce Harmon for suggesting the thesis topic, as well as his continued encouragement and advice, which contributed greatly to the enjoyment of my stay in Iowa. I would also like to thank Dr. Dale Koelling for his hospitality and advice, as well as for supplying a large amount of the computer code needed for the completion of this thesis project. I am indebted to Bill Johansen, George Crabtree, and Fred Schmidt for their prepublication data on the dHvA effect in lutetium. Finally, I would like to thank my friends, who have given much moral support and often helpful advice during the course of my graduate work. I would like to dedicate this thesis to my mother and father, who have continously had faith in me, and who have helped me in so many ways over the years.